ATG9A facilitates the biogenesis of influenza A virus liquid condensates near the ER by dissociating recycling vesicles from microtubules

ATG9A facilitates biogenesis of viral liquid organelles

Sílvia Vale-Costa[1], Temitope Akghibe Etibor[1], Daniela Brás[1], Ana Laura Sousa[2], Maria João Amorim[1,3]*

[1]Cell Biology of Viral Infection Lab, Instituto Gulbenkian de Ciência, Fundação Calouste Gulbenkian, Oeiras, Portugal

[2]Electron Microscopy Facility, Instituto Gulbenkian de Ciência, Fundação Calouste Gulbenkian, Oeiras, Portugal

[3]Cell Biology of Viral Infection Lab, Católica Biomedical Research Centre, Católica Medical School, Universidade Católica Portuguesa, Lisboa, Portugal

Corresponding author*

E-mail: mjamorim@igc.gulbenkian.pt (MJA)

Abstract

Many viruses that threaten public health establish condensates via phase transitions to complete their lifecycles, and knowledge on such processes is key for the design of new antivirals. In the case of influenza A virus, liquid condensates known as viral inclusions are sites dedicated to the assembly of its 8-partite RNA genome. Liquid viral inclusions emerge near the endoplasmic reticulum (ER) exit sites, but we lack the molecular understanding on how the ER contributes to their biogenesis. We show here that viral inclusions develop at remodeled ER sites and display dynamic interactions using the ER, including fusion and fission events and sliding movements. We also uncover a novel role for the host factor, ATG9A, in mediating the exchange of viral inclusions between the ER and microtubules. Depletion of ATG9A arrests viral inclusions at microtubules and prevents their accumulation at the ER, leading to a significantly reduced production of viral genome complexes and infectious virions. In light of our recent findings, we propose that a remodeled ER supports the dynamics of liquid IAV inclusions, with ATG9A acting locally to facilitate their formation. This work advances our current knowledge regarding influenza genome assembly, but also reveals new roles for ATG9A beyond its classical involvement in autophagy.

Introduction

Viruses exploit the cellular architecture and pathways to establish biomolecular condensates that allow the spatiotemporal regulation of processes vital to their biology, such as genome replication and assembly or immune evasion [1]. The influenza A virus (IAV) forms condensates designated viral inclusions, that have been linked to assembly of its genome [2–11]. The IAV genome consists of 8 distinct RNA segments arranged into viral ribonucleoproteins (vRNP), in which the RNA binds the viral RNA-dependent RNA polymerase complex and multiple units of nucleoprotein (NP) [12,13]. Upon nuclear synthesis, progeny vRNPs are exported to the cytosol and assembled into an 8-vRNP complex [12,13], via a poorly characterized process. Evidence supports that genome assembly depends on RNA-RNA interactions between vRNPs and is a selective process as infectious virions contain genomes with precisely 8 different vRNPs [14].

We have recently proposed an appealing model to explain IAV genome assembly [15], which involves the formation of liquid viral inclusions by the process of demixing from the cytosol akin to liquid-liquid phase separation [9]. These condensates form upon expression of a single vRNP type and enlarge as infection progresses, allowing the concentration of vRNPs and facilitating RNA-RNA interactions [9]. By displaying liquid properties (contain no delimiting membrane, are highly dynamic, and internally rearrange) these viral condensates constitute a confined space wherein IAV genome assembly may be efficiently orchestrated [9]. This model is supported by evidence that abrogating the formation [2–4,9–11] or forcing viral inclusions to transition from a liquid into a hardened state [16] efficiently blocks viral production in cellular and animal infection models. It also illustrates that modulating the material state of viral inclusions could become an innovative strategy to control influenza infections.

To abrogate the formation or modulate the material properties of viral inclusions, it is required in-depth understanding of the underlying molecular drivers governing their biogenesis and of the mechanisms regulating their material properties. The only confirmed cellular driver of viral inclusion biogenesis is Rab11a, whose role in IAV genome assembly has been extensively validated [2–4,9–11] (also as reviewed in [15,17,18]). In non-infected cells, Rab11a regulates slow recycling of cargo

to the plasma membrane [19]. During IAV infection, Rab11a was proposed to carry vRNPs to the plasma membrane via the microtubule network [2–7,10]. However, new evidence has refined this model by showing that Rab11a is unavailable to regulate recycling during IAV infection [8]: its movement on microtubules is stalled [20,21], with concomitant accumulation of Rab11a in viral inclusions [8,9]. Importantly, the observation that Rab11a associates with a modified ER during infection [22], together with viral inclusions developing in the vicinity of ER exit sites (ERES) [9], strongly suggests an interplay between the recycling endosome and the ER in IAV genome assembly.

Undoubtedly, the ER is the most common organelle hijacked by many unrelated human relevant viruses, such as coronaviridae and flaviviridae [23,24]. The ER likely facilitates viral propagation owing to its critical and numerous roles in the cell, from protein and lipid synthesis, to carbohydrate metabolism, and calcium storage and signaling [23,24]. In addition, the ER has an expansive membrane able to easily rearrange and to connect with other intracellular organelles [24]. Overwhelming evidence shows that membrane-bound organelles and liquid condensates intimately interact in physiological contexts (as reviewed in [25]). In the case of the ER, it acts as a platform for the phase separation of TIS (TPA-induced sequence) granules, Sec bodies and autophagosome nucleation sites [25,26], but also regulates the fission of liquid ribonucleoprotein granules [27]. Whether the ER plays a role in the biogenesis and dynamics of IAV inclusions and which cellular factors regulate their phase separation at the ER is unknown.

In this study, we sought to better define the interplay between the ER and IAV inclusions, thus providing mechanistic insights into the process of influenza genome assembly. We observed that viral inclusions develop at remodeled ER sites and display dynamic interactions with the ER (fusion and fission events and sliding movements). From an siRNA screen of host factors acting at the ER that impacted IAV infection, we identified ATG9A (autophagy related gene 9A) as a regulator of the trafficking of liquid viral inclusions between the ER and microtubules. In light of our recent findings, we propose that a remodeled ER supports the dynamics of liquid IAV inclusions, with ATG9A acting locally to facilitate their formation.

Results

Viral inclusions dynamically interact with a remodeled ER

We have recently shown that liquid viral inclusions, condensates enriched in Rab11a and vRNPs, develop in the vicinity of the ER subdomain ERES [9]. Others have detected the presence of Rab11a and vRNPs in membranes of a remodeled ER [22]. Why viral inclusions localize to the ER and how these two organelles interact during IAV infection is unclear. One possibility suggested is that the ER is involved in the trafficking of vRNPs [22]. Another hypothesis, which we propose here, is that ER membranes may promote the biogenesis or dynamics of liquid viral inclusions to orchestrate assembly of the 8-vRNP genome. This is also supported by the fact that viral inclusions dissolve if vesicular trafficking between the ER and Golgi is impaired [9].

To first understand the involvement of the ER in the development of viral inclusions, we characterized their ultrastructure in A549 lung epithelial cells expressing low levels of Rab11a wild-type fused to green fluorescent protein (GFP-Rab11a WT^{low}, previously characterized by us [9,28]) and infected with PR8 virus for 12h. We have used these cell lines to identify viral inclusions as cytosolic sites positive for Rab11a and vRNPs, using distinct light and electron imaging methodologies [9,28]. Our previous 2-dimensional (2D) ultrastructural analysis of viral inclusions, using correlative light and transmission electron microscopy, revealed aggregates of double and single membrane vesicles of heterogeneous sizes decorated with vRNPs [9,28]. Another group observed irregularly coated vesicles protruding from a dilated and tubulated ER [22], densely covered with vRNPs and Rab11a. In both studies, ultrastructural analysis was performed using chemical fixation and plastic sectioning, which can introduce artifacts and structural distortions. To consolidate both observations and overcome these methodological limitations, we resolved the 3-dimensional (3D) organization of viral inclusions by high-pressure freezing / freeze substitution and electron tomography transmission electron microscopy (ET-TEM). For 3D model reconstruction, 4 serial tomograms of 120 nm each were stitched together (480 nm thickness in total), of which 3 representative sections are shown (Figs 1A and 1B). The 3D model of an IAV inclusion revealed

numerous single membrane vesicles (smv, green) of heterogeneous size clustered around a double membrane structure (dmv, yellow) that are likely protruding from the ER (er, blue) in infected GFP-Rab11a WT^{low} cells (Figs 1A; S1 and S2 Videos). We also detected the presence of vacuoles (*), which are products of ER lumen enlargement (Fig 1A). In opposition, mock-infected cells had numerous single membrane vesicles near the plasma membrane (pm, gray) or scattered in the cytoplasm, and double membrane vesicles or expanded ER could not be found (Fig 1a; S3 and S4 Videos). The ER features observed in GFP-Rab11a WT^{low} were also present in infected A549 cells, but not in GFP-Rab11a dominant-negative cells (GFP-Rab11a DN^{low}), indicating that they are not an artifact produced as a consequence of Rab11a overexpression (S1 Fig; S5, S6, S7 and S8 Videos).

Fig 1. The remodeled ER supports viral inclusion dynamics during IAV infection. (A) Cells (GFP-Rab11a WT^{low}) were infected or mock-infected with PR8 virus for 12h at a multiplicity of infection (MOI) of 3. Cells were processed by high-pressure freeze / freeze substitution and imaged by electron tomography - transmission electron microscopy (ET-TEM). Representative cells are shown with 3 individual sections and the 3D cumulative model. Bar = 500 nm. Images were extracted from S1, S2, S3 and S4 Videos. Abbreviations: pm, plasma membrane (gray); er, endoplasmic reticulum (blue); v, budding virions (pink); m, mitochondria (purple); smv, single membrane vesicle (green); dmv, double membrane vesicle (yellow). **(B)** Schematic representation of how 4 sequential tomograms (of 120 nm each) were acquired and stitched together. **(C)** Cells (GFP-Rab11a WT^{low}) were infected or mock-infected with PR8 virus for 12h at an MOI of 3. Sections (70 nm) were stained by Tokuyasu double immunogold labeling using antibodies against GFP (18 nm-gold particle to detect Rab11a) and viral NP protein (10 nm-gold particle to detect vRNPs) and imaged by TEM. Green arrowheads show single membrane vesicles (smv), yellow arrowheads highlight double membrane vesicles (dmv) and blue arrowheads point to the ER (er). Bar = 100 nm. **(D)** Cells (GFP-Rab11a WT^{low}, green) were simultaneously transfected with a plasmid encoding mCherry tagged to the ER (magenta) and infected or mock-infected with PR8 virus for 12h at an MOI of 10. Cells were imaged under time-lapse conditions at 12h post-infection (p.i.). Representative cells are shown on the left. The respective individual frames with single moving particles are shown in the small panels

on the right. The yellow arrowheads highlight fusion/fission events of viral inclusions (green), as well as their interaction with the ER (magenta). Bar = 10 μm. Images were extracted from S9 and S10 Videos. **(E)** A linescan was drawn as indicated to assess fusion/fission events of viral inclusions associated with the ER. The fluorescence intensity of ER tubules (magenta) and viral inclusions (green) at indicated times was plotted against the distance (in μm). Analysis was performed using images from (D). Experiments (A-E) were performed twice. For each condition, at least 10 cells were analyzed.

We also confirmed the presence of GFP-Rab11a and vRNPs in viral inclusions by Tokuyasu double immunogold labeling using antibodies against GFP and NP, respectively (Fig 1C). The single membrane vesicles (smv, green arrowhead) stained positive for GFP-Rab11a (18 nm gold particle) and vRNPs (10 nm gold particle), whereas the double membrane vesicles (dmv, yellow arrowhead) stained mostly for vRNPs. It is noteworthy that numerous vRNPs detected inside viral inclusions were not attached to any membrane (Fig 1C). In mock-infected cells, no aggregation of single-membrane vesicles positive for Rab11a was observed, and vRNPs were not detected (Fig 1C).

The proximity of Rab11a and vRNPs to the modified ER is clear from both this and previous studies [2,9,28]. However, how the modified ER relates to viral inclusion formation and regulation of their liquid properties is unknown. To visualize dynamic interactions between liquid viral inclusions and the ER, we performed live imaging of GFP-Rab11a WT^{low} cells (green) transfected with a plasmid encoding mCherry tagged to the ER (magenta) and simultaneously infected or mock-infected with PR8 virus for 12h. As expected, infected GFP-Rab11a WT^{low} cells formed large and rounded viral inclusions that dynamically exchanged material (Fig 1D and S9 Video). We could detect Rab11a on- and off- contacts and sliding movements on the ER, as well as fission and fusion events supported by the ER (Figs 1D and 1E, yellow arrows), similar to those described for vRNPs [9]. In mock-infected cells, Rab11a presents as a tubulovesicular network and, although short-lived contacts between Rab11a and the ER can be occasionally detected, the majority of Rab11a does not localize at the ER (Fig 1C and S10 Video). A similar analysis was not performed in GFP-Rab11a DN^{low} cells, as

viral inclusions do not form in the absence of a functional Rab11a, as we have previously demonstrated [9,28].

Our results suggest that a remodeled ER (double membrane elements, dilated ER) supports the dynamics of liquid viral inclusions.

ATG9A regulates the shape and location of viral inclusions

The above results suggest an intimate link between ER remodeling and the formation or dynamics of IAV inclusions. It is well documented that the ER undergoes complex remodeling during autophagosome biogenesis, ER stress and viral infection [23,29–32]. It is not known, though, how the ER is remodeled and supports the dynamics of IAV inclusions. From an siRNA screening of host factors impacting IAV infection, ATG9A stood out as a putative candidate to explain viral inclusion formation, as this scramblase remodels the ER by supplying membrane from donor organelles like the Golgi or the recycling endosome [33–35]. Although ATG9A was initially identified as a core member of the autophagic machinery, novel roles unrelated to autophagy have been discovered recently, including plasma membrane repair [34], lipid mobilization between organelles [35], and regulation of innate immunity [36]. Mechanistically, ATG9A flips phospholipids between the two membrane leaflets thus contributing to membrane growth [33].

To first test if ATG9A played any role in the development of liquid viral inclusions, A549 cells were treated with siRNA non-targeting (siNT) and targeting ATG9A (siATG9A) for 48h, and subsequently infected with PR8 virus for 8h (Fig 2). Depletion of ATG9A led to a 0.6 log drop in viral titres (Fig 2A, mean $PFU.mL^{-1}$ ± standard error of the mean (SEM): siNT 864289 ± 105127 vs siATG9A 214286 ± 30147) and had a mRNA knockdown efficiency of approximately 85% (Fig 2B, mean relative expression ± SEM: siNT 1.000 ± 0.000 vs siATG9A 0.155 ± 0.025). We confirmed that in mock-infected the major pool of ATG9A (green) colocalized with the Golgi marker GM130 (gray), in agreement with published data [37], and no staining was detected in cells depleted of ATG9A (Fig 2C). However, we could not detect ATG9A subcellular localization in infected cells, which could be due to protein relocalization to unknown sites (Fig 2C).

Fig 2. ATG9A is determinant for the correct shape and distribution of IAV inclusions. Cells (A549) were treated with siRNA non-targeting (siNT) or targeting ATG9 (siATG9A) for 48h and then infected or mock-infected (M) with PR8 virus for 8h, at an MOI of 3. **(A)** Viral production was determined at 8h p.i. by plaque assay and plotted as plaque forming units (PFU) per milliliter (mL) ± standard error of the mean (SEM). Data are a pool from 7 independent experiments. Statistical analysis was done by Mann Whitney test (*p<0.05). **(B)** The mRNA level of ATG9A before infection was quantified by real-time RT-qPCR and plotted as the relative expression to GAPDH mRNA level ± SEM. Expression was normalized to siNT from mock-infected cells. Data are a pool from 7 independent experiments. Statistical analysis was done by Kruskal-Wallis test, followed by a Dunn's multiple comparisons test (*p<0.05, **p<0.01). **(C)** Localisation of host ATG9A (green) and GM130 (gray) and viral NP (magenta) proteins at 8h p.i. was determined by immunofluorescence using antibody staining. Viral inclusions/ vRNPs are highlighted by white boxes. Cell periphery and nuclei (blue, Hoechst staining) are delineated by yellow and white dashed lines, respectively. Bar = 10 µm. **(D)** The roundness and circularity of viral inclusions, marked by NP staining, were determined at 8h p.i. using the Shape Descriptor tool (Image J, NIH) and plotted against each other. The maximum value of roundness and circularity (1) corresponds to a circular structure, whereas the minimum value represents a linear structure (0). More than 80 cells, pooled from 3 independent experiments, were analyzed per condition. Statistical analysis was done by Mann Whitney test (***p<0.001). A schematic representation of shape classification based on circularity versus roundness is also shown. The frequency distribution of roundness and circularity of viral inclusions/ vRNP aggregates is shown in S2A and S2B Fig. **(E, F)** Cells (A549) were transfected with a plasmid encoding mCherry-NP and co-infected with PR8 virus for 8h, at an MOI of 10. Cells were imaged under time-lapse conditions starting at 8h p.i.. White boxes highlight vRNPs/viral inclusions in the cytoplasm in the individual frames. The dashed white and yellow lines mark the cell nucleus and the cell periphery, respectively. The yellow arrows indicate the fission/fusion events and movement of vRNPs/ viral inclusions. Bar = 10 µm. Images were extracted from S11 and S12 Videos. **(G)** The localisation of

host PDI (green) and viral NP (magenta) proteins was determined as described in (C) Bar = 10 µm. Experiments were performed twice.

Alongside the drop in viral production, we also observed an alteration in the shape of viral inclusions, as marked by NP protein (magenta). In control cells, vRNPs aggregated into rounded viral inclusions, but formed instead a tubular network in cells depleted of ATG9A (Fig 2C). To express quantitatively the shape of viral inclusions, we plotted their roundness versus circularity in both experimental conditions (using ImageJ definitions, Fig 2D). The maximum value of circularity (1) corresponds to a perfect circle, whereas smaller values (approaching 0) correspond to shapes with a lower ratio of area to perimeter (long and irregular shapes or rough indented angular surfaces). Roundness (maximum value of 1 and minimum of 0) discriminates structures with circular cross-section from those with different geometric shapes (ellipses, rectangles and irregular shapes). By plotting circularity versus roundness, we could better describe how the shape of viral inclusions changed upon depletion of ATG9A, as illustrated in the schematic representation (Fig 2D; adapted from [38]). The viral inclusions in siNT treated cells had circularity values ranging from 0.39 to 0.80 with 95% confidence interval of [0.59 - 0.63], whereas in siATG9A treated cells values ranged from 0.36 to 0.70 with 95% confidence interval of [0.51 - 0.54] (Fig 2D). The viral inclusions in siNT treated cells had roundness values ranging from 0.60 to 0.73 with 95% confidence interval of [0.65 - 0.66], whereas in siATG9A treated cells values ranged from 0.53 to 0.63 with 95% confidence interval of [0.59 - 0.60] (Fig 2D). Calculation of the frequency distribution of circularity and roundness also clearly showed that viral inclusions in control cells were skewed towards a circular shape, whereas in ATG9A depleted cells they were skewed towards a linear shape (S2A and S2B Figs). This result strongly supports our observation that ATG9A-depleted cells form tubular viral inclusions.

To confirm that tubulation of viral inclusions also occurred in live cells, we treated A549 cells with siNT and siATG9A as above, and then infected with PR8 virus and co-transfected cells with a plasmid coding for viral NP protein fused to a mCherry tag for 8h. This experimental system allowed us to follow movement of vRNPs in live cells, by time-lapse microscopy, as previously published [2,9]. In control cells, we detected exchange of material between rounded viral inclusions supported

by fission and fusion events (Fig 2E, yellow arrows; S11 Video). By contrast, in cells depleted of ATG9A we observed tubules of vRNPs that presented highly dynamic and fast movements (Fig 2F; yellow arrows; S12 Video). Additionally, the association of vRNPs with the ER seen in control cells was lost upon depletion of ATG9A (Fig 2G), as the ER protein PDI (green) no longer surrounded the viral inclusions marked by NP protein (magenta).

In sum, we conclude that the lipid scramblase ATG9A regulates the shape and distribution of liquid IAV inclusions. In the absence of ATG9A, vRNPs do not aggregate into the characteristic rounded viral inclusions interacting with the ER, but instead form a tubular network scattered throughout the cell.

ATG9A is mobilized from the Golgi during IAV infection

Although the major contribution for the expansion of the ERES membrane comes from the ER-Golgi vesicular cycling [29,31,39], whose impairment prevents IAV inclusion formation [9], recent evidence points toward the recycling endosome as an additional ATG9A reservoir and membrane donor compartment [40,41]. Given this, we sought to determine the donor compartment from which ATG9A is mobilized during IAV infection - the Golgi or the recycling endosome [41–43]. Infection with the PR8 virus induced a gradual loss of ATG9A from the Golgi (Fig 3A), as the colocalization between ATG9A and Golgi matrix protein GM130 decreased throughout infection (Figs 3A and 3B, mean ± SEM of Pearson R value: Mock 0.411 ± 0.015, 4h 0.400 ± 0.015, 6h 0.318 ± 0.018, 8h 0.281 ± 0.014, 14h 0.242 ± 0.015). Moreover, we showed that the absence of ATG9A staining at the Golgi at later stages of infection is due to protein relocation and is not due to degradation. As can be appreciated from the western blot (Fig 3C), the total ATG9A protein levels remained constant throughout infection. Numerous ATG9A bands can be observed on the blot, which are likely glycosylated or phosphorylated forms of this protein [44].

Fig 3. ATG9A is mobilized from the Golgi/TGN during IAV infection. (A - C) Cells (A549) were infected or mock-infected with PR8 virus, at an MOI of 3, for the indicated times. **(A)** The localization

of host proteins ATG9A (green) and GM130 (gray) and viral protein NP (magenta) was determined by immunofluorescence using antibodies against these proteins. Mock-infected cells were collected at the same time as the 14h-infected cells. Nuclei (blue, Hoechst staining) and cell periphery are delimited by white and yellow dashed lines, respectively. Bar = 10 µm. **(B)** Colocalization between ATG9A and GM130 in the images acquired in a. was determined using the Colocalization Threshold analysis tool (FIJI/ Image J, NIH) and plotted as the Pearson's R value. Approximately 30 cells, from a single experiment, were analysed per experimental condition. Red bar represents the median of values. Statistical analysis was done by Kruskal-Wallis test (**p>0.01; ***p>0.001). **(C)** The levels of ATG9A, actin and viral NP protein in cell lysates at the indicated time points were determined by western blotting. ATG9A band intensity was quantified using FIJI (ImageJ, NIH) and normalized to actin. Original blots and adjusted brightness and contrast can be found in S1 Raw Images. Experiments (A - C) were performed twice. **(D - F)** Cells (A549) were transfected with a plasmid encoding GFP-ATG9A for 24h and then infected or mock-infected with PR8 virus, at an MOI of 10, for 8h. The localization of endogenous host proteins (GM130 - Golgi, Calnexin - ER or Rab11a - recycling endosome) and viral protein NP was determined by immunofluorescence using antibodies against these proteins. Nuclei (blue or gray, Hoechst staining) and cell periphery are delimited by white and yellow dashed lines, respectively. Yellow arrowheads highlight areas of contact between viral inclusions and overexpressed GFP-ATG9A protein. Red arrowheads highlight areas of colocalization between GFP-ATG9A and the Golgi marker GM130. Bar = 10 µm.

We could not detect the subcellular location of endogenous ATG9A upon leaving the Golgi in infected cells. This could be due to the fact that ATG9A redistribution dilutes protein levels that are harder to detect using antibody staining. Alternatively, we tried to detect the localization of ATG9A in overexpression experiments, by transfecting A549 cells with a plasmid encoding GFP-ATG9A (Figs 3D, 3E and 3F) or GFP (as control, S3 Fig) and infecting them with PR8 virus for 8h. We first confirmed that GFP-ATG9A has a strong localization at the Golgi in mock-infected cells, which significantly decreases with infection (Fig 3D). We also observed that GFP-ATG9A could establish multiple contacts/interaction with viral inclusions, marked by NP and Rab11a, (Fig 3E) in a pattern

315 similar to the one we previously described using ERES markers (Sec16 and Sec31) [9]. Moreover,
316 viral inclusions seemed to be associated with the ER through ATG9A puncta (inset in Fig 3F). Cells
317 overexpressing GFP alone were similarly infected and the morphology or distribution of the ER and
318 Golgi were also not significantly affected (S3 Fig).
319

320 ## ATG9A impacts viral inclusions without affecting the recycling
321 ## endosome

322 Given that the recycling endosome could also be a putative source of ATG9A [40] during infection
323 and that both ATG9A and Rab11a could act in concert to allow the formation of viral inclusions, we
324 tested the effect of depleting ATG9A in cells expressing a functionally active (WT) or inactive (DN)
325 Rab11a. Cells expressing GFP-Rab11a WT^{low} or GFP-Rab11 DN^{low} were treated with siRNA non-
326 targeting (siNT) or targeting ATG9A (siATG9A) for 48h and then infected or mock-infected with PR8
327 virus for 10h. In this case, we explored the link between Rab11a and ATG9A at 10h after infection,
328 as the GFP-Rab11 DN^{low} cells produce low levels of viral particles before this period (by plaque
329 assay), as we have shown before [9]. We observed that the drop in viral titres caused by ATG9A
330 depletion was identical (~0.6 log) in both cell lines, indicating that the effect of ATG9A in IAV infection
331 is independent from Rab11a (Fig 4A, mean $PFU.mL^{-1}$ ± SEM: siNT Rab11a WT 908333 ± 177678,
332 siATG9A Rab11a WT 195000 ± 18394, siNT Rab11a DN 1612 ± 333, siATG9A Rab11a DN 320 ±
333 85). We also confirmed that the efficiency of ATG9A depletion was above 80% for both cell lines (Fig
334 4B, mean relative expression ± SEM: siNT Rab11a WT 1.000 ± 0.000; siATG9A Rab11a WT 0.1040
335 ± 0.051; siNT Rab11a DN 1.102 ± 0.010; siATG9A Rab11a DN 0.172 ± 0.077). However, introducing
336 GFP-Rab11a DN^{low} exogenously in cells resulted in 2.8 log difference (Fig 4A, mean $PFU.mL^{-1}$ ±
337 SEM: siNT Rab11a WT 908333 ± 177678 vs siNT Rab11a DN 1612 ± 333) in viral titres relative to
338 the introduction of GFP-Rab11-WT^{low} as observed before [9].
339

340 **Fig 4. ATG9A impacts viral inclusions via a pathway independent of Rab11a-recycling. (A, B)**
341 Cells (GFP-Rab11a WT^{low} or GFP-Rab11a DN^{low}) were treated with siRNA non-targeting (siNT) or

342 targeting ATG9A (siATG9A) for 48h and then infected or mock-infected with PR8 virus for 10h, at an
343 MOI of 3. **(A)** Viral production was determined by plaque assay and plotted as plaque forming units
344 (PFU) per milliliter (mL) ± standard error of the mean (SEM). Data represent six replicates from a
345 single experiment. Two independent experiments were performed. Statistical analysis was done by
346 one-way ANOVA, followed by a Kruskal-Wallis test (*p<0.05; ***p<0.001). **(B)** The mRNA level of
347 ATG9A before infection was quantified by real-time RT-qPCR and plotted as the relative expression
348 to GAPDH mRNA level ± SEM. Expression was normalized to siNT from mock-infected cells. The
349 data are a pool from 2 independent experiments. Statistical analysis was done by unpaired t-test
350 between siNT versus siATG9A conditions of each condition (WT: mock; WT:PR8; DN: mock; DN:
351 PR8; *p<0.05, **p<0.01). **(C - E)** Cells (A549) were treated with siRNA non-targeting (siNT) or
352 targeting ATG9A (siATG9A) for 48h and then infected or mock-infected with PR8 virus for 8h, at an
353 MOI of 3. **(C)** The localisation of host Rab11a (green) and viral NP (magenta) proteins at 8h p.i. was
354 determined by immunofluorescence using antibody staining. Viral inclusions / vRNPs are highlighted
355 by white boxes. Cell periphery and nuclei (blue, Hoechst staining) are delineated by yellow and white
356 dashed lines, respectively. Bar = 10 µm. Experiments were performed twice. **(D)** Colocalization
357 between Rab11a and NP in the images acquired in (C) was determined using the Colocalization
358 Threshold analysis tool (FIJI/ Image J, NIH) and plotted as the Pearson's R value. At least 20 cells,
359 pooled from 2 independent experiments, were analyzed per experimental condition. Red bar
360 represents the median of values. Statistical analysis was done by Mann-Whitney test (n.s., not
361 significant). **(E)** The roundness and circularity of Rab11a structures were determined using the
362 Shape Descriptor tool (Image J, NIH) and plotted against each other. The maximum value of
363 roundness and circularity (1) corresponds to a circular structure, whereas the minimum value
364 represents a linear structure (0). Approximately 30 cells, from 2 independent experiments, were
365 analyzed per condition. Statistical analysis was done by Mann Whitney test (***p<0.001). The
366 frequency distribution of roundness and circularity of viral inclusions, marked by Rab11a, is shown
367 in S2C and S2D Figs. Experiments were performed twice.
368

We hypothesized that vRNP tubulation caused by ATG9A depletion (Figs 2C, 2D, 2E and 2F) was due to the lack of vRNP association to Rab11a vesicles. To test this, A549 cells were treated with siRNA non-targeting (siNT) or targeting ATG9A (siATG9A) for 48h and then infected or mock-infected with PR8 virus for 8h. The distribution of vRNPs and Rab11a vesicles was detected by immunofluorescence using antibodies against viral NP (magenta) and the host Rab11a (green), respectively. We observed that although ATG9A depletion induced vRNP tubulation, it did not interfere with the association between vRNPs and Rab11a-positive recycling vesicles (Fig 4C), as NP and Rab11a co-localise in both siNT and siATG9A treated cells (Fig 4D, mean Pearson R value ± SEM of: siNT 0.5855 ± 0.02015 vs siATG9A 0.6015 ± 0.0287). The quantification of the circularity versus roundness of viral inclusions, marked by Rab11a, showed that ATG9A depletion also caused tubulation of these structures (Fig 4E), thus matching the previous quantification made using NP (Fig 2D). The viral inclusions in siNT treated cells had circularity values ranging from 0.26 to 0.66 with 95% confidence interval of [0.50 - 0.57], whereas in siATG9A treated cells values ranged from 0.25 to 0.57 with 95% confidence interval of [0.37 - 0.43] (Fig 4E). The viral inclusions in siNT treated cells had roundness values ranging from 0.62 to 0.72 with 95% confidence interval of [0.65 - 0.67], whereas in siATG9A treated cells values ranged from 0.57 to 0.66 with 95% confidence interval of [0.60 - 0.61] (Fig 4E). Calculation of the frequency distribution of circularity and roundness, using Rab11a as marker, also clearly showed that viral inclusions in control cells were skewed towards a circular shape, whereas in ATG9A depleted cells they were skewed towards a linear shape (S2C and S2D Figs).

We conclude that ATG9A is critical for proper establishment of IAV inclusions at the ER but is unlikely to be mobilized from the recycling endosome nor does it influence the association of vRNPs to Rab11a vesicles.

ATG9A impacts the affinity of viral inclusions to microtubules

Our finding that ATG9A depletion induced morphological changes on viral inclusions from circular to tubular (Figs 2C and 2D) that presented high motility (Fig 2E), strongly hinted that viral

inclusions were moving on microtubules. To test if ATG9A influenced the trafficking of vRNPs and Rab11a on microtubules, we performed live cell imaging of GFP-Rab11a WT^{low} cells treated with siRNA non-targeting (siNT) or targeting ATG9A (siATG9) for 48h and then infected or mock-infected with PR8 virus for 8h. Rab11a was used as a proxy to track movement of viral inclusions (magenta), whereas Sir-Tubulin dye was added at the time of infection to visualize microtubules (green). In siNT infected cells, we observed a dynamic but transient movement of Rab11a vesicles on microtubules (Fig 5A; S13 Video). In fact, most of Rab11a exhibited confined random movements, with occasional fast movements that were both processive and saltatory, as expected from previous reports [2,20]. Rab11a vesicles could be seen hopping on and off from the microtubule network (yellow arrows on highlighted inlets), to likely promote the dynamic fusion and fission movements required to form viral inclusions [9]. In siATG9A infected cells, we observed that most Rab11a was moving on microtubules with only few Rab11a vesicles detaching and accumulating in the cytosol (Fig 5B, yellow arrows on highlighted inlets; S14 Video). The data indicate that the high affinity of Rab11a to microtubules in cells depleted of ATG9A confers the tubulated shape observed (Fig 2). In mock-infected cells, fast and short-lived movements of Rab11a vesicles could be traced, regardless of the presence of ATG9A in the cell and no tubulation could be detected (Figs 5C and 5D, S15 and S16 Videos). Quantification of the maximum displacement or the mean squared displacement of viral inclusions over time (Figs 5E, 5F, 5G and 5H), showed that their position significantly deviated more with respect to the reference position in the absence of ATG9A than in the control. This result can be interpreted as viral inclusions spreading faster in the absence of ATG9A and docking less at the ER. Moreover, immunofluorescence data indicate that depletion of ATG9A did not affect the architecture of the microtubule network in either mock-infected or IAV infected cells (Figs 5A, 5B, 5C, 5D and S4A Fig).

Fig 5. ATG9A depletion arrests viral inclusions in microtubules. (A - D) Cells (GFP-Rab11a WT^{low}, magenta) were treated with siRNA non-targeting (siNT) or targeting ATG9A (siATG9A) for 48h. Upon this period, cells were infected or mock-infected with PR8 virus for 8h, at an MOI of 3, and simultaneously treated with 200 nM Sir-Tubulin dye to stain the microtubules (green) in live cells.

Cells were imaged for 10 min (2s / frame) under time-lapse conditions at 8h p.i.. White boxes show viral inclusions / vRNPs. Individual frames with single moving particles highlighted with yellow arrows are shown in the small panels. Bar = 10 μm. Images from selected infected cells were extracted from S13 and S14 Videos. Images from mock-infected cells were extracted from S15 and S16 Video. **(E)** Scheme illustrating how viral inclusion deviation from a reference position (in X and Y direction) was tracked by live cell imaging in infected cells. Formulas used to quantify the mean squared displacement (μm^2) and maximum displacement (μm) are also shown. **(F - H)** Each viral inclusion in a cell (Rab11a as a proxy) was tracked using the TrackMate plugin (FIJI, NIH) and displacement was quantified as explained in (E). Data was plotted as the maximum displacement (μm) per treatment, the mean squared displacement (MSD, μm^2) per treatment, and the average MSD over time (s). For the average MSD over time, particles can be tracked with confidence for a period of 75s, with high deviations/noise beyond that time. The red dot indicates the median in the boxplots. Between 6 - 10 cells per condition were analyzed. Statistical analysis was done by a Kruskal-Wallis test (***$p<0.001$). **(I, J)** Cells (GFP-Rab11a WT^{low}) were treated as explained above (in A - D). At 8h p.i., cells were treated with DMSO or 10 μg/mL of nocodazole for 2h. Cells were imaged at 10h p.i.. White boxes show viral inclusions / vRNPs. Bar = 10 μm. Experiments were performed twice.

To confirm specific trafficking of viral inclusions on microtubules in cells depleted of ATG9A, we performed an experiment as described above and added nocodazole - to induce disassembly of microtubules - 2h before imaging live cells. We observed that in control and infected cells, viral inclusions became larger with little motility upon nocodazole treatment (Fig 5I), as we reported before [9]. Remarkably, in ATG9A depleted and infected cells treated with nocodazole, tubulated viral inclusions also became rounded structures without significant motility (Fig 5I), suggesting that ATG9A depletion caused an arrest of viral inclusions at microtubules. Given that Rab11a is transported on microtubules for normal functions in non-infected cells, we also observed an accumulation of Rab11a in the cytosol of mock-infected cells, regardless of the presence of ATG9A (Fig 5J).

Importantly, we confirmed that ATG9A specifically influenced the movement of viral inclusions on the microtubule network and not on the actin cytoskeleton (S4 Fig). To assess that, cells were treated with siNT or siATG9A and then were infected or mock-infected with PR8 virus for 8h. By immunofluorescence, we stained for actin and microtubules in fixed cells using phalloidin or an antibody against tubulin, respectively. Similarly to our live cell imaging findings, vRNPs also co-localised with tubulin and presented a tubular shape in fixed cells depleted of ATG9A (S4A Fig). We could not detect significant co-localisation of vRNPs on the actin cytoskeleton in either control or ATG9A-depleted cells. Also, ATG9A depletion did not impact the actin cytoskeleton architecture (S4B Fig).

Overall, our findings suggest that ATG9A influences the affinity of viral inclusions to the microtubule network. Although we could not detect the location of endogenous ATG9A during IAV infection, we speculate that ATG9A might promote the transitioning of viral inclusions between microtubules and the modified ER.

ATG9A does not impact virion assembly including genome packaging into virions

Our previous findings showed that ATG9A influences the affinity of viral inclusions to microtubules and their ability to accumulate at the ER. Given that viral inclusions are seen as the putative sites where viral genome assembly takes place, we hypothesized that the arrest of viral inclusions at microtubules caused by ATG9A depletion would affect late steps in the viral lifecycle, such as genome packaging and virion budding. To test this hypothesis, we first quantified the levels of the three viral surface proteins - hemagglutinin (HA), neuraminidase (NA) and matrix protein 2 (M2) - at the plasma membrane of cells treated with siNT or siATG9A and infected or mock-infected with PR8 virus for 8h, using flow cytometry. Using the gating strategy shown (Fig 6A), we observed that depletion of ATG9A led to a significant increase in the levels of the three viral proteins at the plasma membrane (Fig 6A, median fluorescence intensity ± SEM of siNT vs siATG9A: HA - 8674 ± 215 vs 13534 ± 965; NA - 5201 ± 114 vs 7466 ± 28; M2 - 3064 ± 15 vs 5127 ± 386). Accumulation

478 of HA, NA and M2 at the surface in ATG9A depleted cells was not a consequence of a generalized
479 increase in the synthesis of these proteins, as assessed by western blotting (Fig 6B, S1 Raw
480 Images). Given that ATG9A depletion reduces viral production (0.6 log) and increases HA/NA/M2
481 levels (35.9% for HA, 30.3% for NA, 40.2% for M2) at the plasma membrane (Fig 6A), we sought to
482 check if ATG9A depletion was delaying trafficking of vRNPs to the surface or interfering with viral
483 genome assembly by inducing mislocalization of viral inclusions.
484
485 **Fig 6. ATG9A depletion affects viral genome assembly but not packaging.** Cells (A549) were
486 treated with siRNA non-targeting (siNT) or targeting ATG9A (siATG9A) for 48h and then infected or
487 mock-infected with PR8 virus at an MOI of 3. **(A)** The levels of the three viral surface proteins at 8h
488 p.i. (HA, hemagglutinin; NA, neuraminidase; M2, Matrix protein 2) were determined by flow cytometry
489 using monoclonal antibodies against each viral protein and analyzed as shown. The median
490 fluorescence intensity (M.F.I.) of each viral protein at the cell surface was plotted for each
491 experimental condition. Statistical analysis was done by one-way ANOVA, followed by a Sidak's
492 multiple comparisons test (**p<0.01; ***p<0.001). Data are duplicates from a single experiment. Two
493 independent experiments were performed. **(B)** The total levels of the indicated viral and host proteins
494 in cell lysates at 8h p.i. were determined by western blotting. Band intensity was quantified using FIJI
495 (ImageJ, NIH) and normalized to actin. Original blots and adjusted brightness and contrast can be
496 found in S1 Raw Images. **(C, D)** The vRNA copy number per mL for each viral RNA segment (1-8)
497 and the vRNA-to-PFU ratio at 8h p.i. was determined by real-time reverse-transcription quantitative
498 PCR using specific primers as detailed in the methods section. Data are triplicates from a single
499 experiment. Two independent experiments were performed. Statistical analysis was done by a two-
500 way ANOVA test, followed by Bonferroni's multiple comparisons test (*p<0.05; ***p<0.001; n.s, not
501 statistically significant). **(E)** Scheme illustrating that ATG9A is critical for viral inclusion shape and
502 regulates rate of viral genome assembly but does not affect genome packaging into budding virions.
503
504 To ascertain whether ATG9A could affect viral genome packaging, meaning a problem with
505 forming the correct genomes containing 8 different vRNPs, we purified RNA from virions released

into the supernatant of cells treated with siNT or siATG9A for 48h and infected with PR8 virus for 8h. Then, we quantified the number of vRNA copies as well as the vRNA-to-PFU ratio of each viral segment in both conditions. If we observed a problem in genome packaging, the levels of RNA would be similar in both conditions, and it would be expected an increase in vRNA-to-PFU ratio, as reported in [45]. Most vRNA segments had decreased copy numbers in cells depleted of ATG9A, with the exception of segments 5 and 6 (Fig 6C). Although there were modest differences in the vRNA-to-PFU ratio of most viral RNA segments, they were not statistically significant (Fig 6D). Overall, both results indicate that there was not a major defect in the incorporation of the 8 vRNA segments in virions in the absence of ATG9A .

Taken together, these data suggest that ATG9A is likely involved in the regulation of viral inclusion distribution, facilitating circulation between microtubules and the ER. By interfering with viral inclusion trafficking, viral genome assembly and delivery to budding sites at the plasma membrane may be delayed or decreased, thus causing accumulation of HA, NA and M2 at the surface. ATG9A may thus be a host catalyst that facilitates viral genome assembly (Fig 6E).

Discussion

The importance of phase transitions to viral lifecycles has become evident in recent years, and knowledge on these processes may foster the design of innovative antivirals [1]. Many viruses that threaten public health establish biomolecular condensates via phase transitions to fulfill critical steps in their lifecycles [1]. In the case of IAV infection, the viral inclusions with liquid properties arising by a yet uncharacterized process [9,16] and responding similarly to condensates described to form by liquid-liquid phase separation [1,25] are viewed as key sites dedicated to viral genome assembly. Here, vRNPs concentrate and facilitate viral intersegment interactions [9,16,28]. Our present work contributes towards current knowledge regarding IAV genome assembly by uncovering a host factor, ATG9A, that mediates the exchange of viral inclusions between microtubules and the ER (Fig 7). ATG9A contributes to the spatial distribution of viral inclusions and thus the ability of their main components, Rab11a and vRNPs, to demix from the cytosol (presumably by liquid phase separation) at remodeled ER membranes. Whether the subcellular targeting of vRNPs using cellular machinery and the cytoskeleton allows vRNPs to reach the saturation concentration enabling liquid phase separation remains unknown [1]. Relevant to this field in general, is to understand how exactly the transport of components regulates formation and activity of biomolecular condensates.

Fig 7. Proposed model for ATG9A role in the establishment of liquid IAV inclusions. We hypothesize that liquid viral inclusions, composed of Rab11a membranes and viral ribonucleoproteins (vRNPs), might be the sites dedicated to the assembly of the influenza A virus genome [9,15,28]. These structures behave as liquid compartments, having the ability to engage in fission and fusion events to facilitate the exchange of vRNPs and thus promote assembly of complete complexes of 8 vRNPs (segments 1 to 8) [9]. In this study, we showed that viral inclusions develop in close contact with a remodeled endoplasmic reticulum (ER) containing double-membrane rearrangements. Moreover, we identified a host factor, ATG9A, which we propose to act as a linker that facilitates the exchange of viral inclusions between the ER and microtubules. We identified that

ATG9A is mobilized from the Golgi during IAV infection to establish multiple and dynamic contacts with viral inclusions. It is possible that ATG9A moves to the ER to promote the linkage of viral inclusions to microtubules.

This work highlights that ATG9A is a versatile component able to organize vesicular trafficking in ways that drive formation and activity of liquid condensates by limiting access to microtubules. This finding allocates a new function to the myriad of newly identified roles for ATG9A [26,34,35,46–49] beyond its well-known involvement in autophagy [30,33,37,50,51]. Recent studies support that ATG9A may be a key regulator of vesicular trafficking. ATG9A functions in protein export from the *trans*-Golgi network (TGN) [47], regulation of neurite outgrowth [48], in coupling autophagosome biogenesis to synaptic vesicle cycling [49], and chemotactic migration [46]. It is also involved in plasma membrane repair [34], lipid mobilization between organelles [35], as well as in the regulation of innate immunity [36]. These studies also show that ATG9A has a wide subcellular distribution according to the specific function being executed.

In this study, we found that ATG9A is mobilized from the Golgi/TGN during IAV infection (Figs 3A, 3B and 3D) and establishes highly dynamic contacts with viral inclusions and the ER (Figs 3F, and 3E). This interaction between ATG9A and viral inclusions was only detectable upon overexpression of ATG9A (Figs 3F, and 3E), which is a limitation of our study. We observed though that depleting ATG9A caused an arrest of viral inclusions at microtubules (Figs 5A and 5B) and consequent loss of their association with the ER (Fig 2G). Our experimental setting did not allow us to determine the directionality of viral inclusion movement, that is, if ATG9A controls the exit of viral inclusions from microtubules to the ER or if when we deplete ATG9A, we create an artificial way to introduce vRNPs in microtubules, that does not relate to infection. However, the impact that ATG9A has in viral production fits the first option better. Still in both cases, this work shows that in the context of infection, the dissociation of viral inclusions from microtubules is a regulated process and not a competition between vRNPs and molecular motors for binding to Rab11a, as initially proposed by us

and others [4,20,28,52,53]. In this sense, ATG9A could catalyze the passage of viral inclusions to alternative transport means or locations such as the ER [9,22].

Given the highly dynamic nature of ATG9A and its ability to supply proteins and lipids from the Golgi (e.g. phosphoinositide-metabolizing enzymes) [37,54], ATG9A may create ER microdomains favorable for phase separation of viral inclusions. This is in line with our previous finding that blocking the ER-Golgi vesicular cycling abolished the formation of liquid viral inclusions [9]. Although it was proposed that the recycling endosome is the primary reservoir of ATG9A for autophagosome initiation [40], we found that the main pool of ATG9A mobilized during IAV infection originated from the Golgi/TGN (Fig 2C, 3A). Moreover, we showed that ATG9A does not interfere with the co-transport of Rab11a and vRNPs (Fig 4C and 4D) but may promote sites for their accumulation, creating opportunities for the establishment of interactions amongst them and hence propel their demixing from the cytosol. We cannot exclude, however, the possibility that ATG9A interacts with other regulators of the recycling endosome, such as Rab11b and Rab10.

The concept that ATG9A is a modulator of liquid-liquid phase separation on or near ER in mammalian cells has also been recently proposed by another group [26]. ATG9A regulates phase separation and spatial organization of the autophagosome component FIP200 on the ER tubules. Interestingly, FIP200 condensates associate and move along the ER strand and enlarge via growth or fusion, with ATG9A dynamically orbiting FIP200 condensates in a manner similar to viral inclusions (Fig 3D, 3E and 3F).

Whether ATG9A acts directly to locally coordinate phase separation of viral inclusions, or indirectly via its lipid scramblase activity to remodel the ER is yet to be determined. In fact, several ATGs have been implicated in ER remodeling in other viral infections, specifically in the formation of double membrane vesicles [23]. While coronaviridae and flaviviridae exploit ER composition and structure to form viral organelles enabling viral RNA replication, assembly and evasion from immune detection [23,24,55], orthomyxoviridae viruses such as IAV possibly use it for genome assembly as replication occurs in the nucleus. Viral strategies identified for ER remodeling by coronaviridae and

599 flaviviridae include co-opting of ER-shaping proteins [56] and exploitation of cellular pathways such
600 as autophagy [57] and lipid metabolism [58,59], but no such strategies have been identified for IAV.

601 How condensates move within cells has not been widely explored. A remodeled ER could
602 create a favorable environment where cellular machinery (as ATG9A) would support phase
603 separation of viral inclusions (Fig 1A), thus enabling efficient spatiotemporal coordination of IAV
604 genome assembly. It is well described that the ER forms contacts with the membranes of many other
605 organelles to modulate their biogenesis and dynamics, including liquid phase separated organelles
606 (TIS granules, Sec and P-bodies, omegasomes) [25,27,60]. Here, we found that during infection
607 Rab11a condensates displayed transient and highly dynamic movements at the ER (Fig 1D and 1E).
608 These movements included fusion, fission and sliding on the surface of the ER, similar to those that
609 we had described before for vRNPs [9]. Additionally, a remodeled ER may support other steps of the
610 viral lifecycle. In fact, ER membranes have been proposed to transport progeny vRNPs to the plasma
611 membrane for viral packaging [22]. Alterations in ER shape in IAV infection could alternatively be
612 linked to exploitation of lipid metabolism, deregulation of cell-autonomous immunity or ER stress
613 pathways [61].

614 Understanding the mechanisms controlling the material properties of viral inclusions formed
615 during IAV infection may provide new means to prevent IAV genome assembly. Future directions
616 should involve identifying the interacting partners of ATG9A and the signaling pathways that promote
617 phase separation of viral inclusions at the ER. It will also be critical to define the molecular basis of
618 ER remodeling in infection and learn whether this process can be targeted to block IAV infection.
619 The unveiled key biological processes may have extended relevance to other severe viral infections
620 which involve ER remodeling and phase separation, for example hepatitis C virus and SARS-CoV-
621 2.

Materials and methods

Metadata access. All metadata is deposited in https://doi.org/10.5281/zenodo.7418724.

Cells and Viruses. The human epithelial cells Madin-Darby Canine Kidney (MDCK) and alveolar basal (A549) were a kind gift of Prof Paul Digard, Roslin Institute, UK. The GFP-Rab11 WT and DN stable cell lines (in A549 background) were previously produced and characterized by us [9,28]. All cell types were cultured in Dulbecco's Modified Eagle's medium (DMEM, Gibco, 21969035) supplemented with 10 % fetal bovine serum (FBS, Gibco, 10500064), 1% penicillin / streptomycin solution (Biowest, L0022) and 2 mM L-glutamine (Gibco). GFP-Rab11 WT and DN cell culture media was also supplemented with 1.25 µg mL^{-1} puromycin (Calbiochem). Cells were regularly tested for mycoplasma contamination with the LookOut mycoplasma PCR detection kit (Sigma, MP0035), using JumpStart Taq DNA Polymerase (Sigma, D9307). Reverse-genetics derived A/Puerto Rico/8/34 (PR8 WT; H1N1) was used as a model virus and titrated by plaque assay according to reference [28]. Virus infections were performed at a multiplicity of infection (MOI) of 3 to 10. After 45 min, cells were overlaid with DMEM containing 0.14% bovine serum albumin (BSA). To calculate viral titres, supernatants collected from infected cells were subjected to a plaque assay on MDCK monolayers. The drug nocodazole (Sigma, 487928) was dissolved in DMSO and used at a final concentration of 10 µg mL^{-1} for 2h.

Plasmids and siRNA. Reverse genetic plasmids were contributed by Dr Ron Fouchier (Erasmus MC, Netherlands). The mCherry-tagged NP plasmid was a kind gift from Prof Paul Digard (Roslin Institute, UK) and the GFP-tagged ATG9A plasmid was a gift from Dr Sharon Tooze (Francis Crick Institute, UK). The plasmid encoding mCherry tagged to the ER was produced in-house and characterized in [9]. The siRNA targeting ATG9A (mixture of 4 siRNAs, GS79065, #1027416) and non-targeting (NT, # 5091027310) were purchased from Qiagen.

Transfections. For plasmid transfection, cells were grown to 70% confluency in 24-well plates and transfected with 250 ng of indicated plasmids using Lipofectamine LTX and Opti-MEM (both from Life Technologies), according to manufacturer's instructions. Cells were simultaneously transfected and infected or mock-infected with PR8, at MOI 10, for 8h. Specifically for GFP-ATG9A overexpression, plasmid transfection was performed 24h before infection. For siRNA transfection, cells were grown to 50% confluency in 6-well plates the day before transfection. Cells were transfected with siRNA (100 pmol/well) using DharmaFECT (Dharmacon) for 48h, and then infected or mock-infected with PR8 at MOI 3 for 8h.

High-pressure freezing/ Freeze substitution and Electron Tomography. Cells grown on 3 mm aclar disks (carbon coated) were fixed using a mixture of 2% (v/v) formaldehyde and 0.2% (v/v) glutaraldehyde (Polysciences) in 0.1M phosphate buffer, for 2h at RT. Cells in the aclar disks were added to a 0.04 mm deep carrier filled with 1-hexadecene and frozen using a High Pressure Freezer Compact 02 (Wohlwend Engineering Switzerland). The samples were then freeze substituted at -90ºC with 0.1% (w/v) uranyl acetate and 0.01% (w/v) tannic acid (EMS) in acetone for 6h using a Leica EM AFS2 with a processor Leica EM FSP. The temperature was then raised to -45ºC at a slope of 5ºC/h. Samples were stabilized at -45ºC for 1.5h before washing in acetone three times. Samples were infiltrated and embedded in Lowicryl HM20 (Polysciences) at -45ºC. Polymerization of the resin was done using UV light at -25ºC for 48h. Sections of 120 nm (Leica UC7) were picked on palladium-copper grids coated with 1% (w/v) formvar (Agar Scientific) in chloroform (VWR). The post-staining was made with 1% (w/v) uranyl acetate and Reynolds lead citrate, for 5 minutes each. For tomography, 15 nm protein A-gold (UMC, Utrecht) was added to both sides of the sections before staining, as fiducial markers. Tomograms were acquired on a FEI Tecnai G2 Spirit BioTWIN operating at 120 keV equipped with a Olympus-SIS Veleta CCD Camera. Images were aligned based on the fiducial markers. Electron tomograms were reconstructed and joined with the IMOD software package. Manual segmentation of the area of interest was employed to generate 3D models using the AMIRA software (Thermo Scientific).

Tokuyasu—double immunogold labeling. Cells were fixed in suspension using 2% (v/v) formaldehyde (EMS) and 0.2% (v/v) glutaraldehyde (Polysciences) in 0.1 M Phosphate buffer (PB), for 2 h at RT. Subsequently, cells were centrifuged and washed with PB. The aldehydes were quenched using 0.15% (w/v) glycine (VWR) in 0.1 M PB for 10 min at RT. Cells were infiltrated in 12% (w/v) gelatin (Royal) for 30 min at 37 °C and centrifuged. The gelatin was solidified on ice, cut into 1 mm^3 cubes and placed in 2.3 M sucrose (Alfa Aesar) in 0.1 M PB, overnight at 4 °C. The cubes were mounted onto specimen holders and frozen at −196 °C by immersion into liquid nitrogen. Samples were trimmed and cut into 50-nm-thick sections (in a Leica EM-FC7 at −110 °C) and laid onto formvar-carbon coated 100-mesh grids. For immunogold labeling, sections were blocked with PBS/1% BSA for 20 min at RT. Antibody staining was done sequentially in PBS/1% BSA at RT: rabbit anti-GFP (1:500, 1 h, Abcam, 6556), goat anti-rabbit IgG conjugated to 18 nm gold (1:20, 30 min; Jackson ImmunoResearch Laboratories, 111-215-144), mouse anti-NP (1:200, 1 h, Abcam, 20343), and goat anti-mouse IgG conjugated with 6 nm gold (1:20, 30 min; Jackson ImmunoResearch Laboratories, 115-195-146). Gold particles were fixed by applying 1% (v/v) formaldehyde in PBS for 5 min at RT. Blocking and extensive washing were performed in-between stainings. In the final step, gold particles were fixed using 1% (v/v) glutaraldehyde (Polysciences) for 5 min RT. Grids were washed in distilled H2O and counterstained using methyl-cellulose–uranyl acetate solution for 5 min on ice. EM images were acquired on a Hitachi H-7650 operating at 100 keV equipped with a XR41M mid mount AMT digital camera. Images were post-processed using Adobe Photoshop CS5 and ImageJ (NIH).

Fixed-cell imaging. For immunofluorescence, cells were fixed for 15 min with 4% formaldehyde and permeabilized for 7 min with 0.2% (v/v) Triton-X-100 in PBS. Cells were incubated with the indicated primary antibodies for 1 h at RT, washed and incubated for 45 min with Alexa fluor conjugated secondary antibodies and Hoechst. Antibodies used were: rabbit polyclonal against Rab11a (1:200; Proteintech, 15903-1-AP), ATG9 (1:200, Abcam, 108338) and viral NP (1:1000; gift from Prof Paul Digard, Roslin Institute, UK); mouse monoclonal against viral NP (1:1000; Abcam, 20343), PDI (1:500, Life Technologies, MA3-019), GM130 (1:500, BD Transduction Laboratories, 610823); rat

monoclonal against alpha-tubulin (1:200; YL1/2, Santa Cruz Biotechnologies, sc-53029). Actin was stained using 100 nM of phalloidin-iFluor488 for 30 min, RT (Phalloidin-iFluor 488 Reagent (ab176753). Secondary antibodies were all from the Alexa Fluor range (1:1000; Life Technologies). Following washing, cells were mounted with Dako Faramount Aqueous Mounting Medium and single optical sections were imaged with a SP5 live confocal microscope (Leica) or LSM 980 with AiryScan super-resolution microscope (Zeiss). For size and shape quantifications of viral inclusions, images were converted to 8-bit color, background was removed, threshold adjusted and "shape descriptor" function was used to determine the roundness/circularity of each viral inclusion inside selected cells using ImageJ (NIH). Frequency distributions were calculated and plotted with GraphPad Prism using intervals of circularity/roundness values between [0-1]. Images were post-processed using Adobe Photoshop CS2 and ImageJ (NIH).

Live-cell imaging. Cells (2 x 10^4 / well) were grown in chambered glass-bottomed dishes (Lab-Tek) and maintained at 37°C, 5% CO_2 in Opti-MEM medium (Gibco) during imaging. Samples were imaged using Roper TIRF Spinning Disk (Yokogawa CSU-X1) or LSM 980 with AiryScan super-resolution microscope (Zeiss) and post-processed using Adobe Photoshop CS2 and ImageJ (NIH). For microtubule staining in live cells (5x10^4), 200 nM of Sir-Tubulin (Cytoskeleton, Inc) was added 10h before imaging. Trackmate plugin (ImageJ, NIH) was used to track viral inclusions for 10 min at a timescale of 2 s/frame in live cells and XY trajectories were subsequently analyzed in a custom R (version 4.1.0) script.

Western blotting. Western blotting was performed according to standard procedures and imaged using a LI-COR Biosciences Odyssey near-infrared platform. Antibodies used included: rabbit polyclonal against virus PB1 (1:500), PB2 (1:200), PA (1:500), NP (1:1000), all antibodies were a kind gift by Prof. Paul Digard, Roslin Institute, UK); mouse monoclonal against NS1 (neat, clone 1A7) and HA (neat, clone H36-26), both antibodies were a kind gift from Dr Jonathan Yewdell, Cellular Biology Section Laboratory of Viral Diseases (NIAID, NIH); mouse monoclonal against M2 (1:500, clone 14C2, Abcam, 5416), rabbit polyclonal against ATG9A (1:500, Abcam, 108338); mouse

polyclonal against actin (1:1000; Sigma, A5441). The secondary antibodies used were from the IRDye range (1:10000; LI-COR Biosciences). The original uncropped blots are included in the S1 Raw Images.

Fluorescence activated cell sorting. Cell monolayers (6 x 10^6) were trypsinized for 7 min at 37ºC, centrifuged at 1500 rpm for 5 min and cell pellets were resuspended in PBS containing 2% FBS. Approximately 1 x 10^6 cells / well were incubated for 30 min on ice with either PBS or with a monoclonal mouse antibody against viral proteins HA (neat, clone 6F6, produced in-house), NA (neat, clone 7D8, produced in-house) and M2 (1:400, clone 14C2, Abcam, 5416). Cells were then washed with PBS / 2% FBS and centrifuged at 1500 rpm for 5 min for 3 consecutive rounds. Cells were then either incubated with PBS or with a secondary antibody against mouse IgG conjugated to Alexa 568 (1:1000, Life Technologies). Several steps of washing and centrifugation were performed to remove the unbound antibody. Upon washing with PBS / 2% FBS, cells were fixed with 2% paraformaldehyde (2% PFA) at RT for 15 min, washed again in PBS and analyzed in a BD Fortessa X-20 flow cytometer equipped with 4 lasers 405 nm, 488 nm, 561 nm e 640 nm; a SSC detector and 16 detectors 6V, 2A, 5A-V and 3V.

Quantitative real-time reverse-transcription PCR (RT-qPCR). Extraction of RNA from samples in NZYol (NZYtech, MB18501) was achieved by using the Direct-zol RNA minipreps (Zymo Research, R2052). Reverse transcription (RT) was performed using the transcriptor first strand cDNA kit (Roche, 04896866001). Real-time RT-PCR to detect GAPDH and ATG9 was prepared in 384-well, white, thin walled plates 384-well PCR Plate (ABgene 12164142) by using SYBR Green Supermix (Biorad, 172-5124), 10% (v/v) of cDNA and 0.4 µM of each primer. The reaction was performed on a ABI QuantStudio-384 machine (Applied Biosciences), under the following PCR conditions: Cycle 1 (1 repeat): 95 °C for 2 min; Cycle 2 (40 repeats): 95 °C for 5 s and 60 °C for 30 s; Cycle 3: 95 °C for 5 s and melt curve 65 °C to 95 °C (increment 0.05 °C each 5 s). Standard curves were prepared by serially diluting 1:5 a mock-infected sample from each experiment. Data were analyzed using the QuantStudio 7 software (Applied Biosciences). The mRNA level of host factors was quantified

760 relative to reference GAPDH mRNA level. Expression was normalized to siNT from mock-infected
761 cells treated with control siRNA. Primer sequences used for real-time RT-qPCR are listed in S1 Data.
762
763 ***In vitro* synthesis of vRNA standards.** The strategy used in this study was published by [60]. The
764 primers used to create templates containing a T7 phage promoter (TAATACGACTCACTATAGGG)
765 sequence are listed in S1 Data. Viral gene sequences in pPolI plasmids for all PR8 segments were
766 amplified by PCR using corresponding primer pairs and were purified using ZYMO Research DNA
767 cleaner and Concentrator-5 (ZYMO, D4014). Purified PCR products were *in vitro* transcribed using
768 the T7 RiboMAX Express Large Scale RNA Production System (Promega, P1320). The transcripts
769 were purified using the RNeasy Micro kit (QIAGEN, 74004). The concentration of purified RNA was
770 determined by spectrophotometry. The molecular copies of synthetic RNA were calculated based on
771 the total molecular weight of the segment.
772
773 **RNA extraction from virions.** Supernatants from virus-infected cells were centrifuged at 6800g for
774 3min to clear cryoprecipitates. Virion RNA was extracted using the QIAamp Viral RNA Mini kit
775 (Qiagen, 52906) according to manufacturer's instructions. The concentration of purified RNA was
776 determined by use of spectrophotometry.
777
778 **Hot-start reverse transcription with a tagged primer.** cDNAs complementary to vRNA (standards
779 and RNA isolated from virions) were synthesized with tagged primers to add an 18–20 nucleotide
780 tag at the 5′ end that was unrelated to influenza virus (vRNAtag, GGCCGTCATGGTGGCGAAT).
781 Reverse transcription with the tagged primer was performed with the hot-start modification of using
782 saturated trehalose, as described in [60].
783
784 **vRNA-to-PFU ratio quantification.** Absolute quantification of vRNA levels in isolated virions was
785 done by real-time RT-PCR as described above. Standard curves were generated by 100-fold serial
786 dilutions of synthetic viral RNA. Data were analyzed using the QuantStudio software (Applied
787 Biosciences). Primer sequences used for reverse transcription and for real-time RT-qPCR are listed

788 in S1 Data. The ratio of vRNA levels to plaque forming units (vRNA-to-PFU) was calculated by
789 dividing vRNA levels in isolated virions by the PFUs obtained from the same cell supernatants.
790
791 **Data quantification and statistical analysis.** Data were analyzed in Prism 6 version (GraphPad
792 Software) and in R (version 4.1.0). Experimental replicates and tests applied to determine statistical
793 significance between different conditions are described in each figure legend.
794

Acknowledgments

The authors acknowledge Prof Paul Digard (Roslin Institute, UK), Dr Ron Fouchier (Erasmus MC, Netherlands) and Dr Sharon Tooze (Francis Crick Institute) for providing cells and reagents. The authors thank Dr Marta Alenquer (CBR, Portugal) and Dr Caitlin Simpson (University of Bristol, UK) for critical reading of the manuscript.

References

[1] Etibor TA, Yamauchi Y, Amorim MJ. Liquid Biomolecular Condensates and Viral Lifecycles: Review and Perspectives. Viruses 2021;13:366. https://doi.org/10.3390/v13030366.

[2] Amorim MJ, Bruce EA, Read EKC, Foeglein Á, Mahen R, Stuart AD, et al. A Rab11- and Microtubule-Dependent Mechanism for Cytoplasmic Transport of Influenza A Virus Viral RNA. J Virol 2011;85:4143–56. https://doi.org/10.1128/JVI.02606-10.

[3] Eisfeld AJ, Kawakami E, Watanabe T, Neumann G, Kawaoka Y. RAB11A Is Essential for Transport of the Influenza Virus Genome to the Plasma Membrane. J Virol 2011;85:6117–26.

[4] Momose F, Sekimoto T, Ohkura T, Jo S, Kawaguchi A, Nagata K, et al. Apical transport of influenza A virus ribonucleoprotein requires Rab11-positive recycling endosome. PLoS One 2011;6:e21123.

[5] Avilov SV, Moisy D, Munier S, Schraidt O, Naffakh N, Cusack S. Replication-Competent Influenza A Virus That Encodes a Split-Green Fluorescent Protein-Tagged PB2 Polymerase Subunit Allows Live-Cell Imaging of the Virus Life Cycle. J Virol 2012;86:1433–48.

[6] Chou Y-Y, Heaton NS, Gao Q, Palese P, Singer R, Lionnet T. Colocalization of Different Influenza Viral RNA Segments in the Cytoplasm before Viral Budding as Shown by Single-molecule Sensitivity FISH Analysis. PLoS Pathog 2013;9:e1003358.

[7] Lakdawala SS, Wu Y, Wawrzusin P, Kabat J, Broadbent AJ, Lamirande EW, et al. Influenza a virus assembly intermediates fuse in the cytoplasm. PLoS Pathog 2014;10:e1003971.

[8] Vale-Costa S, Alenquer M, Sousa AL, Kellen B, Ramalho J, Tranfield EM, et al. Influenza A virus ribonucleoproteins modulate host recycling by competing with Rab11 effectors. J Cell Sci 2016;129:1697–710.

[9] Alenquer M, Vale-Costa S, Etibor TA, Ferreira F, Sousa AL, Amorim MJ. Influenza A virus ribonucleoproteins form liquid organelles at endoplasmic reticulum exit sites. Nat Commun 2019;10:1629. https://doi.org/10.1038/s41467-019-09549-4.

[10] Bruce EA, Digard P, Stuart AD. The Rab11 pathway is required for influenza A virus budding and filament formation. J Virol 2010;84:5848–59.

[11] Han J, Ganti K, Sali VK, Twigg C, Zhang Y, Manivasagam S, et al. Host factor Rab11a is critical for efficient assembly of influenza A virus genomic segments. PLoS Pathog 2021;17:e1009517.

[12] Eisfeld AJ, Neumann G, Kawaoka Y. At the centre: influenza A virus ribonucleoproteins. Nat Rev Microbiol 2015;13:28–41.

[13] Ferhadian D, Contrant M, Printz-Schweigert A, Smyth RP, Paillart J-C, Marquet R. Structural and Functional Motifs in Influenza Virus RNAs. Front Microbiol 2018;9:559. https://doi.org/10.3389/fmicb.2018.00559.

[14] Li X, Gu M, Zheng Q, Gao R, Liu X. Packaging signal of influenza A virus. Virol J 2021;18:36. https://doi.org/10.1186/s12985-021-01504-4.

[15] Amorim MJ. A Comprehensive Review on the Interaction Between the Host GTPase Rab11 and Influenza A Virus. Front Cell Dev Biol 2019;6:176. https://doi.org/10.3389/fcell.2018.00176.

[16] Etibor TA, Vale-Costa S, Sridharan S, Brás D, Becher I, Mello VH, et al. Rules for hardening influenza A virus liquid condensates. BioRxiv 2022:2022.08.03.502602. https://doi.org/10.1101/2022.08.03.502602.

[17] Staller E, Barclay WS. Host Cell Factors That Interact with Influenza Virus Ribonucleoproteins. Cold Spring Harb Perspect Med 2020.

[18] Vale-Costa S, Amorim MJ. Recycling Endosomes and Viral Infection. Viruses 2016;8:64.

[19] O'Sullivan MJ, Lindsay AJ. The Endosomal Recycling Pathway—At the Crossroads of the Cell. Int J Mol Sci 2020;21:6074.

[20] Bhagwat AR, Le Sage V, Nturibi E, Kulej K, Jones J, Guo M, et al. Quantitative live cell imaging reveals influenza virus manipulation of Rab11A transport through reduced dynein association. Nat Commun 2020;11:23.

[21] Ganti K, Han J, Manicassamy B, Lowen AC. Rab11a mediates cell-cell spread and reassortment of influenza A virus genomes via tunneling nanotubes. PLOS Pathog 2021;17:e1009321. https://doi.org/10.1371/journal.ppat.1009321.

[22] de Castro Martin IF, Fournier G, Sachse M, Pizarro-Cerda J, Risco C, Naffakh N. Influenza virus genome reaches the plasma membrane via a modified endoplasmic reticulum and Rab11-dependent vesicles. Nat Commun 2017;8:1396. https://doi.org/10.1038/s41467-017-01557-6.

[23] Wolff G, Melia CE, Snijder EJ, Bárcena M. Double-Membrane Vesicles as Platforms for Viral Replication. Trends Microbiol 2020;28:1022–33. https://doi.org/10.1016/j.tim.2020.05.009.

[24] Ravindran MS, Bagchi P, Cunningham CN, Tsai B. Opportunistic intruders: how viruses orchestrate ER functions to infect cells. Nat Rev Microbiol 2016;14:407–20. https://doi.org/10.1038/nrmicro.2016.60.

[25] Zhao YG, Zhang H. Phase Separation in Membrane Biology: The Interplay between Membrane-Bound Organelles and Membraneless Condensates. Dev Cell 2020;55:30–44. https://doi.org/10.1016/j.devcel.2020.06.033.

[26] Zheng Q, Chen Y, Chen D, Zhao H, Feng Y, Meng Q, et al. Calcium transients on the ER surface trigger liquid-liquid phase separation of FIP200 to specify autophagosome initiation sites. Cell 2022. https://doi.org/10.1016/j.cell.2022.09.001.

[27] Lee JE, Cathey PI, Wu H, Parker R, Voeltz GK. Endoplasmic reticulum contact sites regulate the dynamics of membraneless organelles. Science 2020;367:eaay7108. https://doi.org/10.1126/science.aay7108.

[28] Vale-Costa S, Alenquer M, Sousa AL, Kellen B, Ramalho J, Tranfield EM, et al. Influenza A virus ribonucleoproteins modulate host recycling by competing with Rab11 effectors. J Cell Sci 2016:jcs.188409. https://doi.org/10.1242/jcs.188409.

[29] Grasso D, Renna FJ, Vaccaro MI. Initial Steps in Mammalian Autophagosome Biogenesis. Front Cell Dev Biol 2018;6:146.

[30] Karanasios E, Walker SA, Okkenhaug H, Manifava M, Hummel E, Zimmermann H, et al. Autophagy initiation by ULK complex assembly on ER tubulovesicular regions marked by ATG9 vesicles. Nat Commun 2016;7:12420.

[31] Staiano L, Zappa F. Hijacking intracellular membranes to feed autophagosomal growth. FEBS Lett 2019;593:3120–34.

[32] Xu F, Du W, Zou Q, Wang Y, Zhang X, Xing X, et al. COPII mitigates ER stress by promoting formation of ER whorls. Cell Res 2021;31:141–56. https://doi.org/10.1038/s41422-020-00416-2.

886 [33] Matoba K, Kotani T, Tsutsumi A, Tsuji T, Mori T, Noshiro D, et al. Atg9 is a lipid scramblase that
887 mediates autophagosomal membrane expansion. Nat Struct Mol Biol 2020;27:1185–93.
888 https://doi.org/10.1038/s41594-020-00518-w.
889 [34] Claude-Taupin A, Jia J, Bhujabal Z, Garfa-Traoré M, Kumar S, da Silva GPD, et al. ATG9A
890 protects the plasma membrane from programmed and incidental permeabilization. Nat Cell Biol
891 2021;23:846–58. https://doi.org/10.1038/s41556-021-00706-w.
892 [35] Mailler E, Guardia CM, Bai X, Jarnik M, Williamson CD, Li Y, et al. The autophagy protein ATG9A
893 enables lipid mobilization from lipid droplets. Nat Commun 2021;12:6750.
894 https://doi.org/10.1038/s41467-021-26999-x.
895 [36] Saitoh T, Fujita N, Hayashi T, Takahara K, Satoh T, Lee H, et al. Atg9a controls dsDNA-driven
896 dynamic translocation of STING and the innate immune response. Proc Natl Acad Sci
897 2009;106:20842–6. https://doi.org/10.1073/pnas.0911267106.
898 [37] Judith D, Jefferies HBJ, Boeing S, Frith D, Snijders AP, Tooze SA. ATG9A shapes the forming
899 autophagosome through Arfaptin 2 and phosphatidylinositol 4-kinase IIIβ. J Cell Biol
900 2019;218:1634–52.
901 [38] Ismaiel HAH, Askalany MM, Ali AI. Evaluation of white silica sands in North Eastern Desert,
902 Egypt. Int J Sci Eng Res 2017;8:1713–22.
903 [39] Ge L, Zhang M, Kenny SJ, Liu D, Maeda M, Saito K, et al. Remodeling of ER-exit sites initiates
904 a membrane supply pathway for autophagosome biogenesis. EMBO Rep 2017;18:1586–603.
905 [40] Puri C, Vicinanza M, Ashkenazi A, Gratian MJ, Zhang Q, Bento CF, et al. The RAB11A-Positive
906 Compartment Is a Primary Platform for Autophagosome Assembly Mediated by WIPI2
907 Recognition of PI3P-RAB11A. Dev Cell 2018;45:114-131.e8.
908 [41] Longatti A, Tooze SA. Recycling endosomes contribute to autophagosome formation.
909 Autophagy 2012;8:1682–3.
910 [42] Young ARJ, Chan EYW, Hu XW, Köchl R, Crawshaw SG, High S, et al. Starvation and ULK1-
911 dependent cycling of mammalian Atg9 between the TGN and endosomes. J Cell Sci
912 2006;119:3888–900.

913 [43] Orsi A, Razi M, Dooley HC, Robinson D, Weston AE, Collinson LM, et al. Dynamic and transient
914 interactions of Atg9 with autophagosomes, but not membrane integration, are required for
915 autophagy. Mol Biol Cell 2012;23:1860–73.
916 [44] Xie, Y., Kang, R., Sun, X., Zhong, M., Huang, J., Klionsky, D. J., & Tang, D. Posttranslational
917 modification of autophagy-related proteins in macroautophagy. Autophagy 2015;11:28–45.
918 https://doi.org/doi.org/10.4161/15548627.2014.984267.
919 [45] Hutchinson Edward C., Curran Martin D., Read Eliot K., Gog Julia R., Digard Paul. Mutational
920 Analysis of cis-Acting RNA Signals in Segment 7 of Influenza A Virus. J Virol 2008;82:11869–
921 79. https://doi.org/10.1128/JVI.01634-08.
922 [46] Campisi D, Desrues L, Dembélé K-P, Mutel A, Parment R, Gandolfo P, et al. The core autophagy
923 protein ATG9A controls dynamics of cell protrusions and directed migration. J Cell Biol
924 2022;221:e202106014. https://doi.org/10.1083/jcb.202106014.
925 [47] Jia S, Wang Y, You Z, Liu B, Gao J, Liu W. Mammalian Atg9 contributes to the post-Golgi
926 transport of lysosomal hydrolases by interacting with adaptor protein-1. FEBS Lett
927 2017;591:4027–38. https://doi.org/10.1002/1873-3468.12916.
928 [48] Yamaguchi J, Suzuki C, Nanao T, Kakuta S, Ozawa K, Tanida I, et al. Atg9a deficiency causes
929 axon-specific lesions including neuronal circuit dysgenesis. Autophagy 2018;14:764–77.
930 https://doi.org/10.1080/15548627.2017.1314897.
931 [49] Yang S, Park D, Manning L, Hill SE, Cao M, Xuan Z, et al. Presynaptic autophagy is coupled to
932 the synaptic vesicle cycle via ATG-9. Neuron 2022;110:824-840.e10.
933 https://doi.org/10.1016/j.neuron.2021.12.031.
934 [50] Sawa-Makarska J, Baumann V, Coudevylle N, von Bülow S, Nogellova V, Abert C, et al.
935 Reconstitution of autophagosome nucleation defines Atg9 vesicles as seeds for membrane
936 formation. Science 2020;369:eaaz7714. https://doi.org/10.1126/science.aaz7714.
937 [51] van Vliet AR, Chiduza GN, Maslen SL, Pye VE, Joshi D, De Tito S, et al. ATG9A and ATG2A
938 form a heteromeric complex essential for autophagosome formation. Mol Cell 2022.
939 https://doi.org/10.1016/j.molcel.2022.10.017.

940 [52] Veler Hana, Fan Haitian, Keown Jeremy R., Sharps Jane, Fournier Marjorie, Grimes Jonathan
941 M., et al. The C-Terminal Domains of the PB2 Subunit of the Influenza A Virus RNA Polymerase
942 Directly Interact with Cellular GTPase Rab11a. J Virol 2022;96:e01979-21.
943 https://doi.org/10.1128/jvi.01979-21.
944 [53] Kawaguchi A, Hirohama M, Harada Y, Osari S, Nagata K. Influenza Virus Induces Cholesterol-
945 Enriched Endocytic Recycling Compartments for Budozone Formation via Cell Cycle-
946 Independent Centrosome Maturation. PLoS Pathog 2015;11:e1005284.
947 [54] Judith D, Tooze SA. ATG9A supplies PtdIns4P to the autophagosome initiation site. Autophagy
948 2019;15:1660–1.
949 [55] Zhang J, Lan Y, Sanyal S. Membrane heist: Coronavirus host membrane remodeling during
950 replication. Biochimie 2020;179:229–36. https://doi.org/10.1016/j.biochi.2020.10.010.
951 [56] Rajah MM, Monel B, Schwartz O. The entanglement between flaviviruses and ER-shaping
952 proteins. PLOS Pathog 2020;16:e1008389. https://doi.org/10.1371/journal.ppat.1008389.
953 [57] Dinesh Kumar N, Smit JM, Reggiori F. Strategies employed by viruses to manipulate autophagy.
954 Prog Mol Biol Transl Sci 2020;172:203–37.
955 [58] Strating JR, van Kuppeveld FJ. Viral rewiring of cellular lipid metabolism to create membranous
956 replication compartments. Curr Opin Cell Biol 2017;47:24–33.
957 https://doi.org/10.1016/j.ceb.2017.02.005.
958 [59] Altan-Bonnet N. Lipid Tales of Viral Replication and Transmission. Trends Cell Biol
959 2017;27:201–13. https://doi.org/10.1016/j.tcb.2016.09.011.
960 [60] Wu H, Carvalho P, Voeltz GK. Here, there, and everywhere: The importance of ER membrane
961 contact sites. Science 2018;361:eaan5835. https://doi.org/10.1126/science.aan5835.
962 [61] Mazel-Sanchez B, Iwaszkiewicz J, Bonifacio JPP, Silva F, Niu C, Strohmeier S, et al. Influenza
963 A viruses balance ER stress with host protein synthesis shutoff. Proc Natl Acad Sci
964 2021;118:e2024681118. https://doi.org/10.1073/pnas.2024681118.
965 [62] Kawakami E, Watanabe T, Fujii K, Goto H, Watanabe S, Noda T, et al. Strand-specific real-time
966 RT-PCR for distinguishing influenza vRNA, cRNA, and mRNA. J Virol Methods 2011;173:1–6.
967 https://doi.org/10.1016/j.jviromet.2010.12.014.
968

Supporting information captions

S1 Fig. IAV inclusions form in A549 infected cells but do not form in the absence of a functionally active Rab11a. Cells (A549 and GFP-Rab11a DN^{low}) were infected with PR8 virus for 12h, at an MOI of 3. Cells were processed by high-pressure freeze / freeze substitution and imaged by electron tomography - transmission electron microscopy (ET-TEM). In each case, 4 sequential tomograms (of 120 nm each) were acquired and stitched together. Representative cells are shown with individual sections and the 3D cumulative model. For each condition, at least 10 cells were analysed. Bar = 500 nm. Images were extracted from S5, S6, S7 and S8 Video. Abbreviations: pm, plasma membrane; er, endoplasmic reticulum; v, budding virions; m, mitochondria; smv, single membrane vesicle; dmv, double membrane vesicle.

S2 Fig. ATG9A depletion elongates viral inclusions. Cells (A549) were treated with siRNA non-targeting (siNT) or targeting ATG9A (siATG9A) for 48h and then infected, at an MOI of 3, with PR8 virus for 8h. Cells were fixed and analysed by immunofluorescence using an antibody against viral NP protein **(A, B)** or host Rab11 **(C, D)**. The (A, C) roundness and (B, D) circularity of viral inclusions, as marked by viral NP protein, were calculated for each condition using the Shape Descriptor tool (Image J, NIH) and were plotted as the percentage of a binned frequency distribution as shown. The maximum value of roundness and circularity (1) corresponds to a circular structure, whereas the minimum value represents a linear structure (0). More than 80 cells, from 3 independent experiments, were analyzed per condition. Statistical analysis was done by two-way ANOVA, followed by a Sidak's multiple comparisons test (***p<0.001, **p<0.01).

S3 Fig. GFP overexpression effect on infection and ER/Golgi is identical to GFP-ATG9A overexpression. Cells (A549) were transfected with a plasmid encoding GFP (as control for GFP-ATG9A) for 24h and then infected or mock-infected with PR8 virus, at an MOI of 10, for 8h. The localization of endogenous host proteins (GM130 - Golgi or Calnexin - ER) and viral protein NP was

996 determined by immunofluorescence using antibodies against these proteins. Nuclei (blue or gray,
997 Hoechst staining) and cell periphery are delimited by white and yellow dashed lines, respectively.
998 Bar = 10 µm.
999
1000 **S4 Fig. ATG9A affects viral inclusion movement on microtubules, but not on actin**
1001 **cytoskeleton. (A, B)** Cells (A549) were treated with siRNA non-targeting (siNT) or targeting ATG9A
1002 (siATG9A) for 48h and then infected, at an MOI of 3, with PR8 virus for 8h. The localization of tubulin
1003 (green) and viral protein NP (magenta) was determined by immunofluorescence using antibodies
1004 against these proteins. The distribution of actin filaments was done by staining with the dye phalloidin
1005 Alexa Fluor 488 (green). Nuclei (blue, Hoechst staining) and cell periphery are delimited by white
1006 and yellow dashed lines, respectively. Viral inclusions are highlighted in white boxes. Bar = 10 µm.
1007

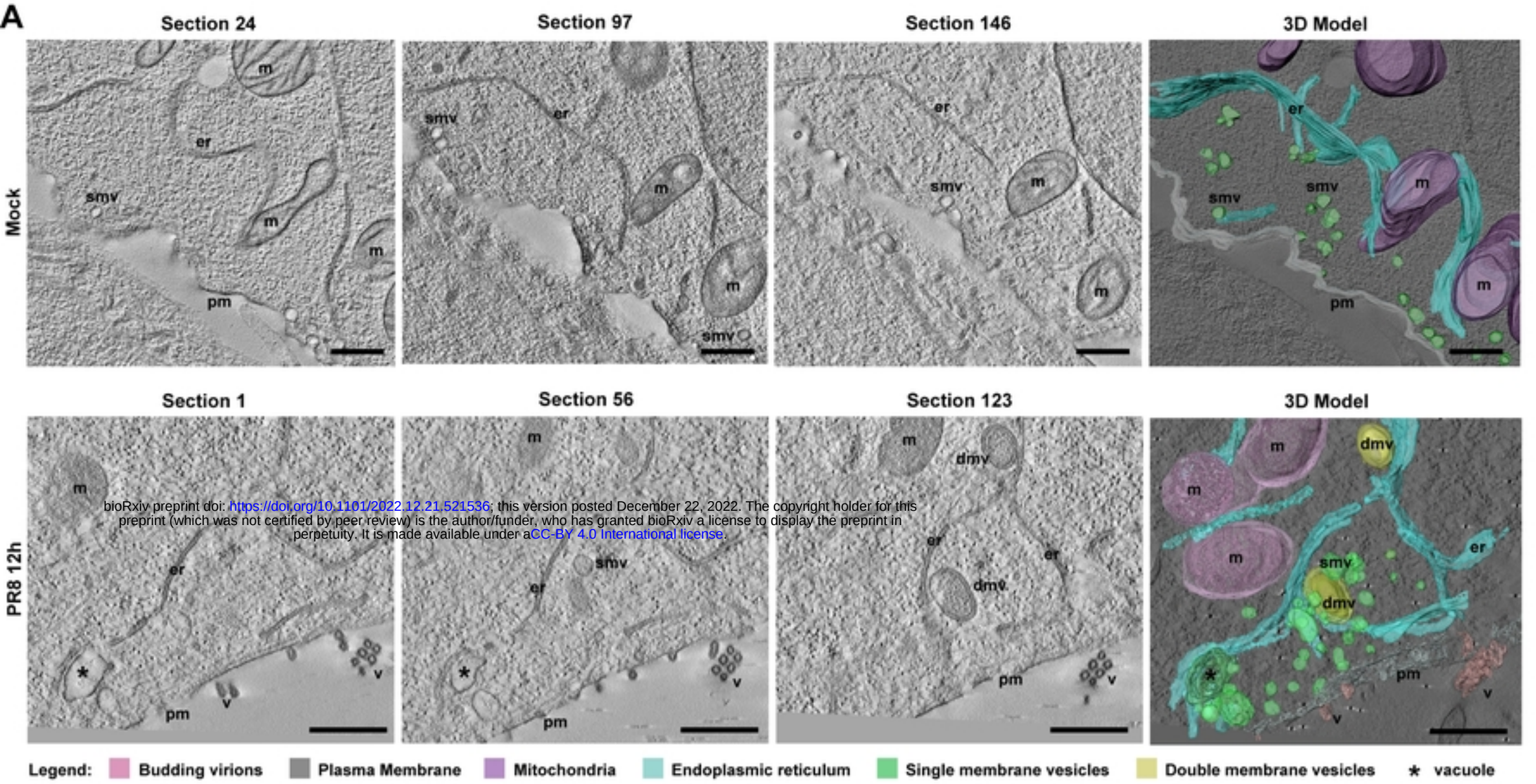

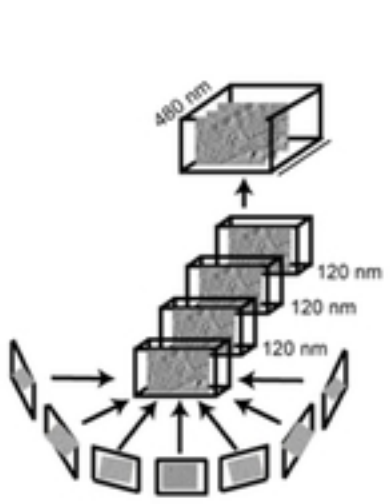

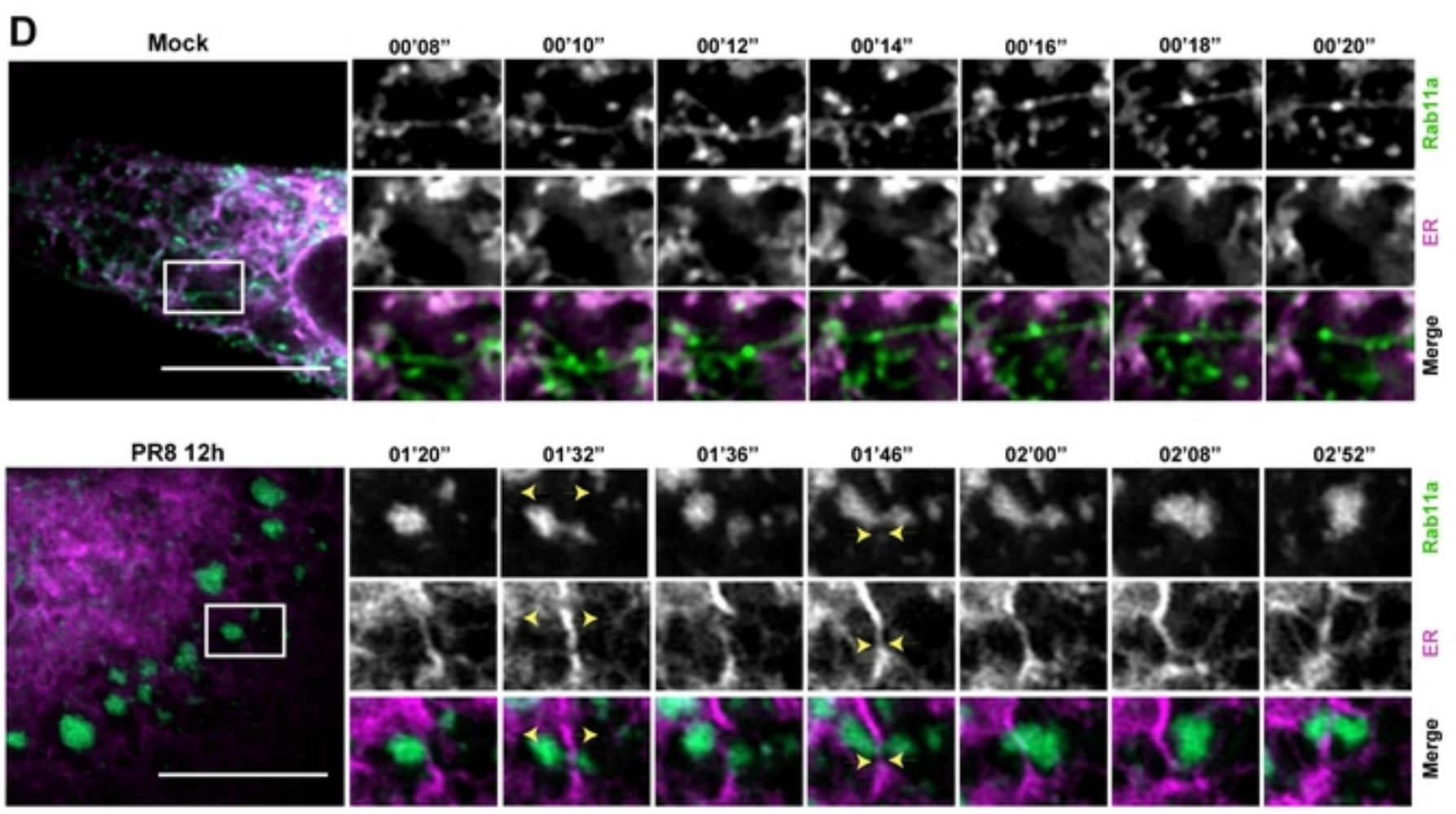

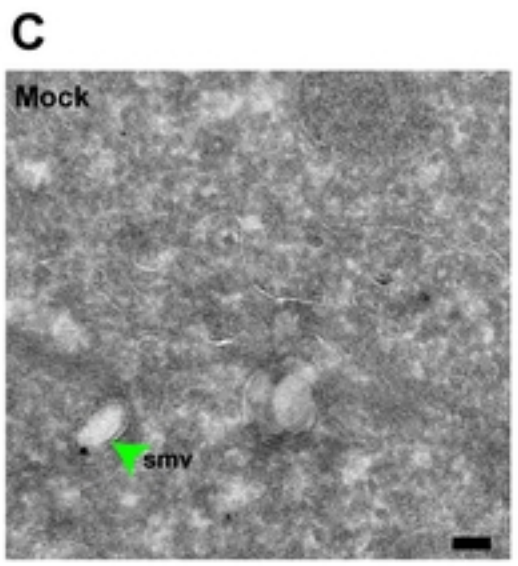

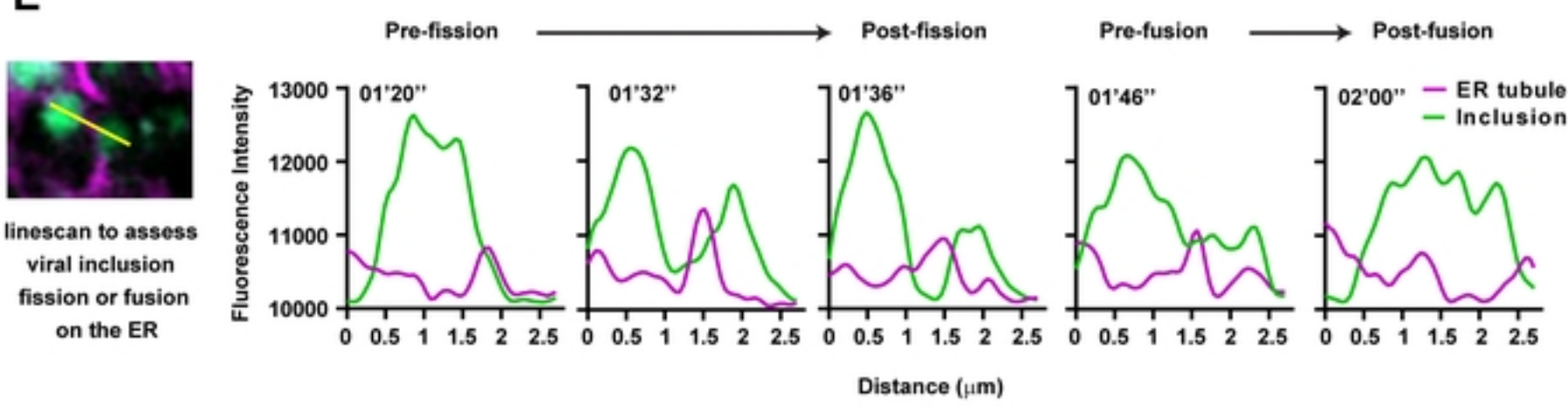

Figure 1

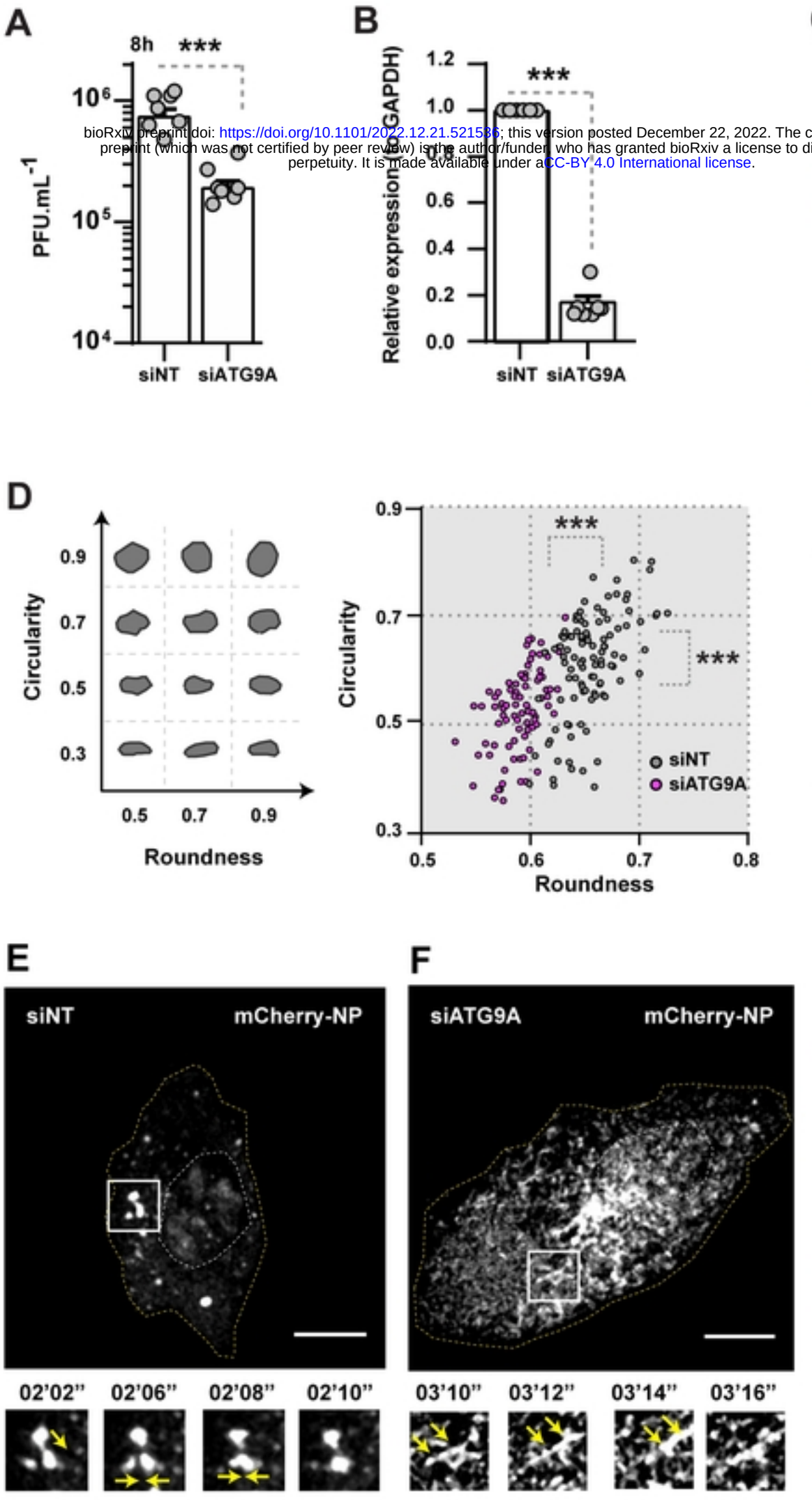

Figure 2

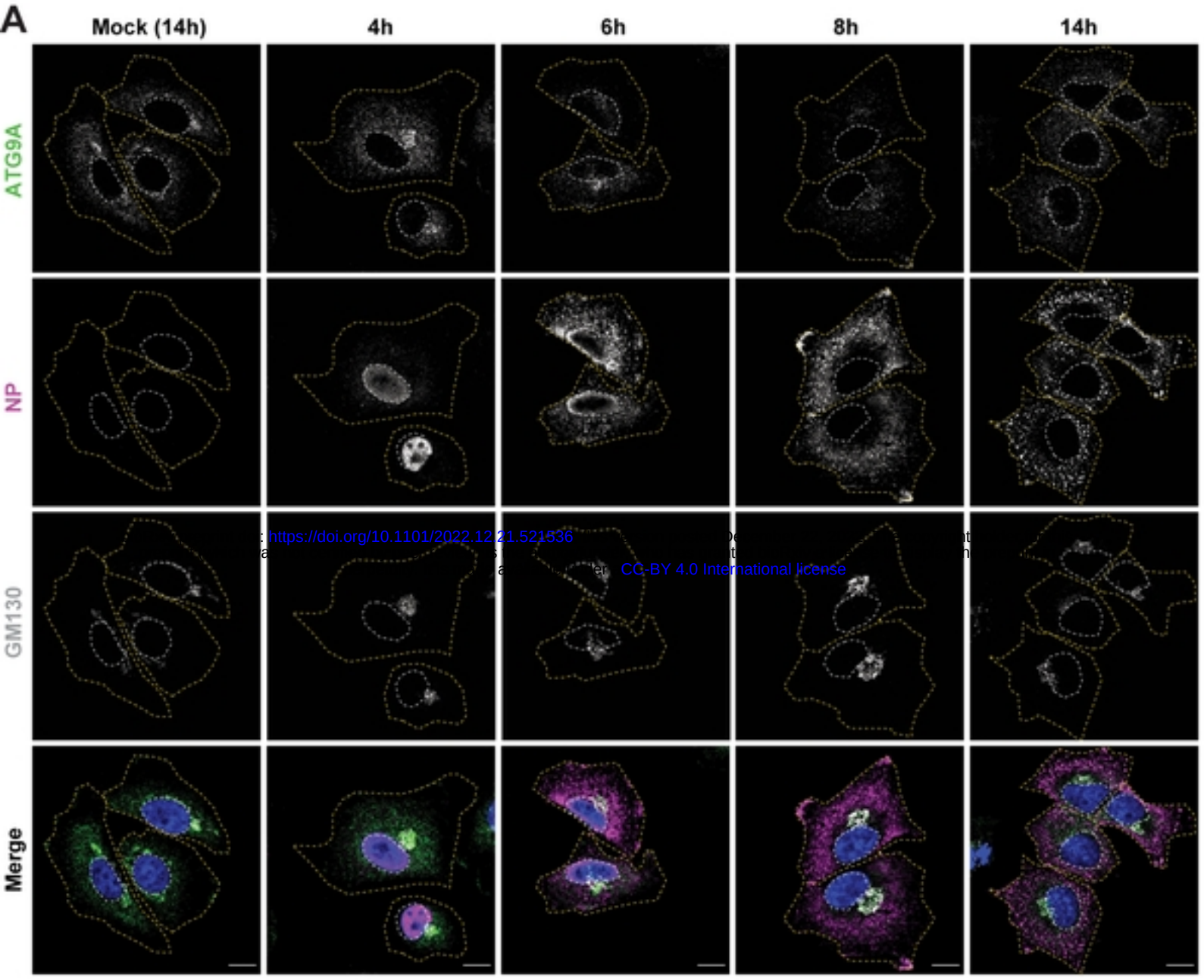

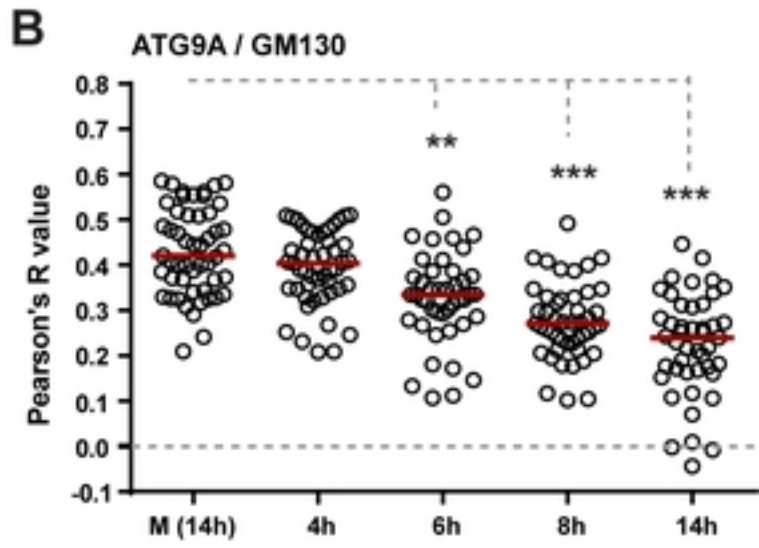

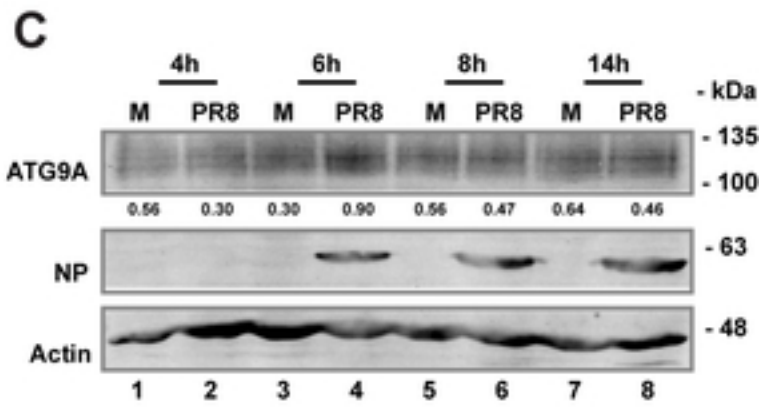

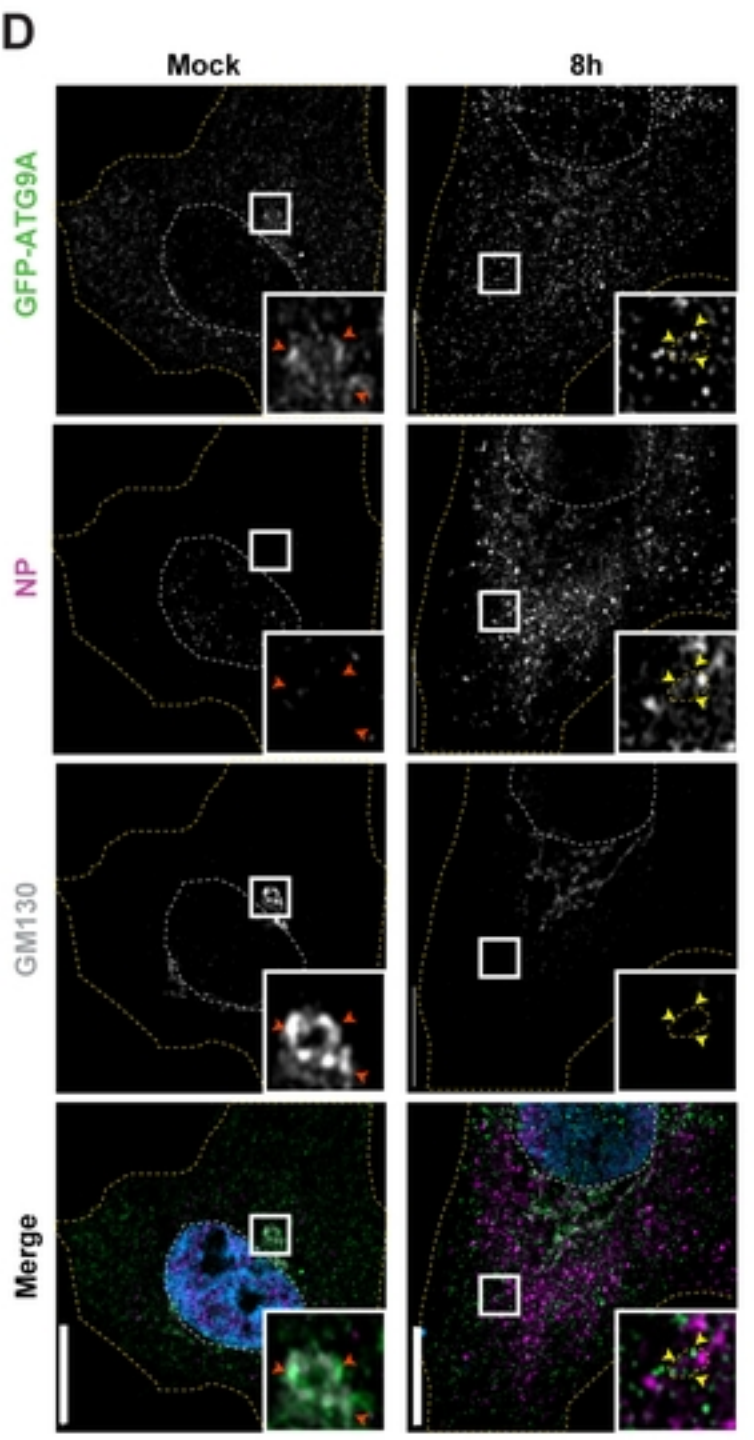

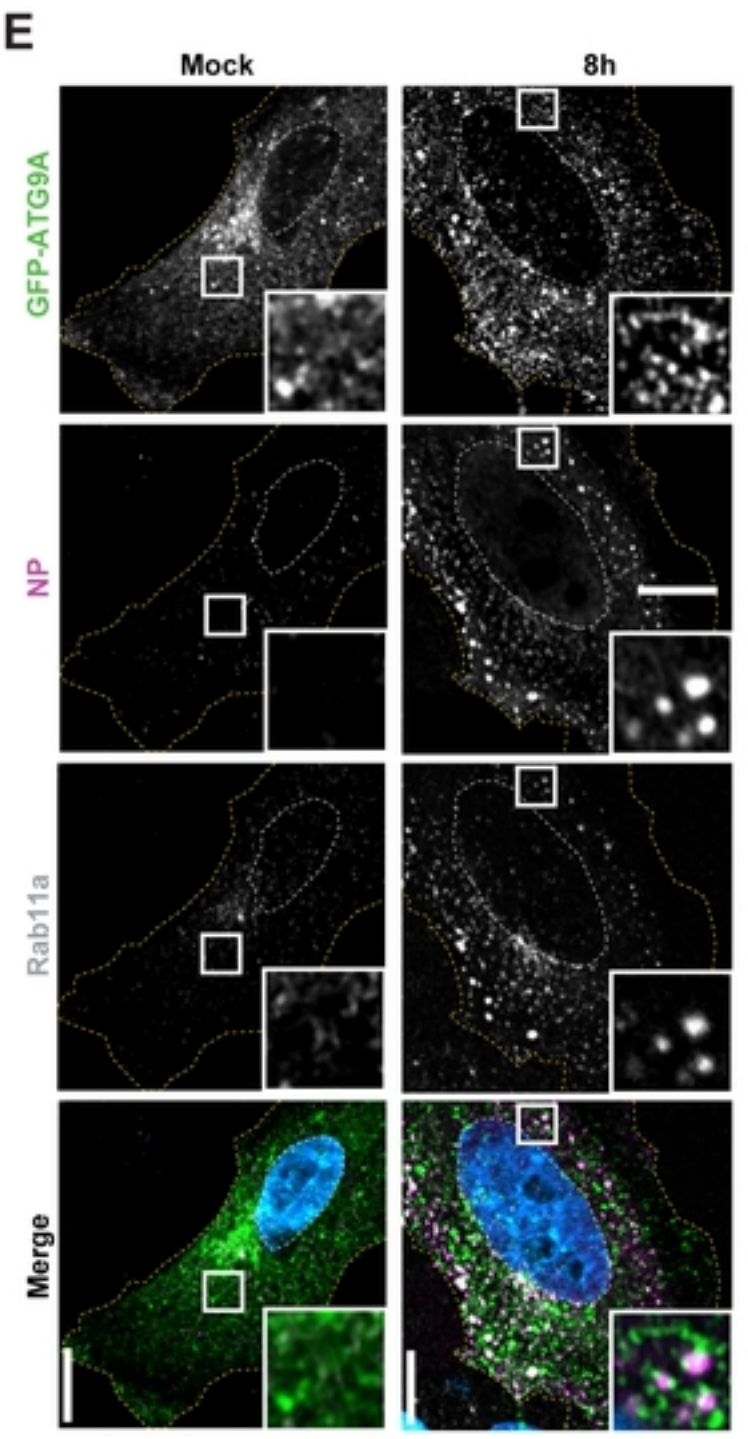

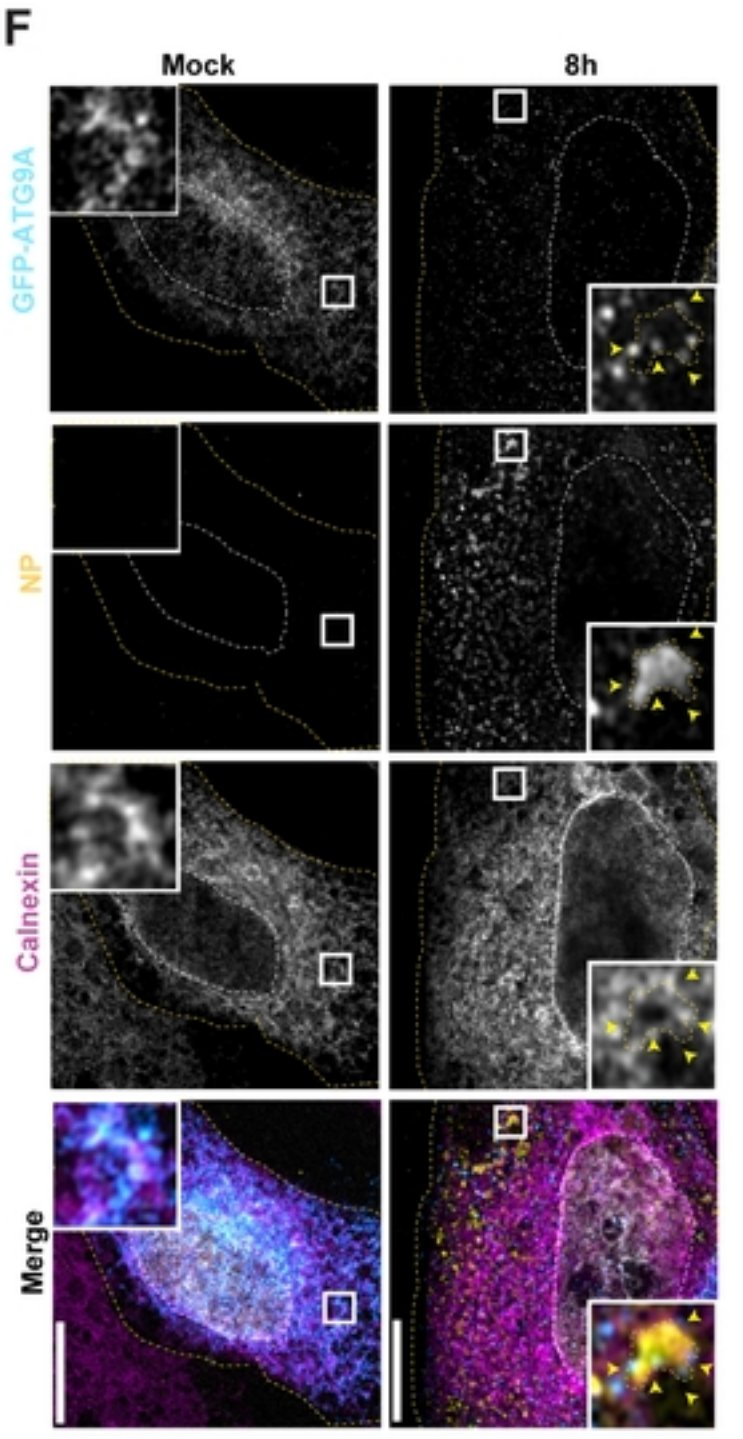

Figure 3

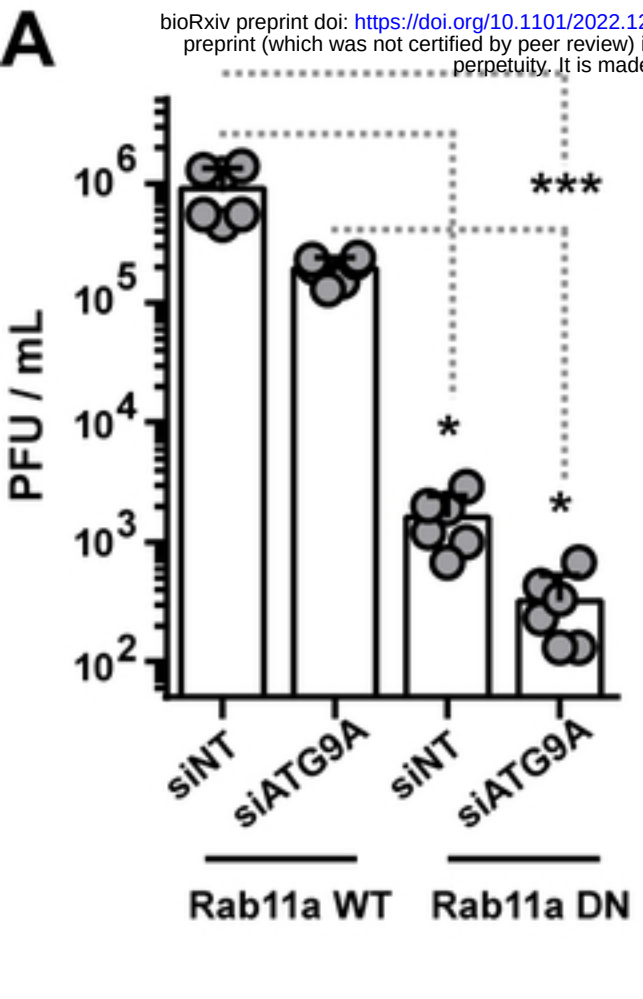

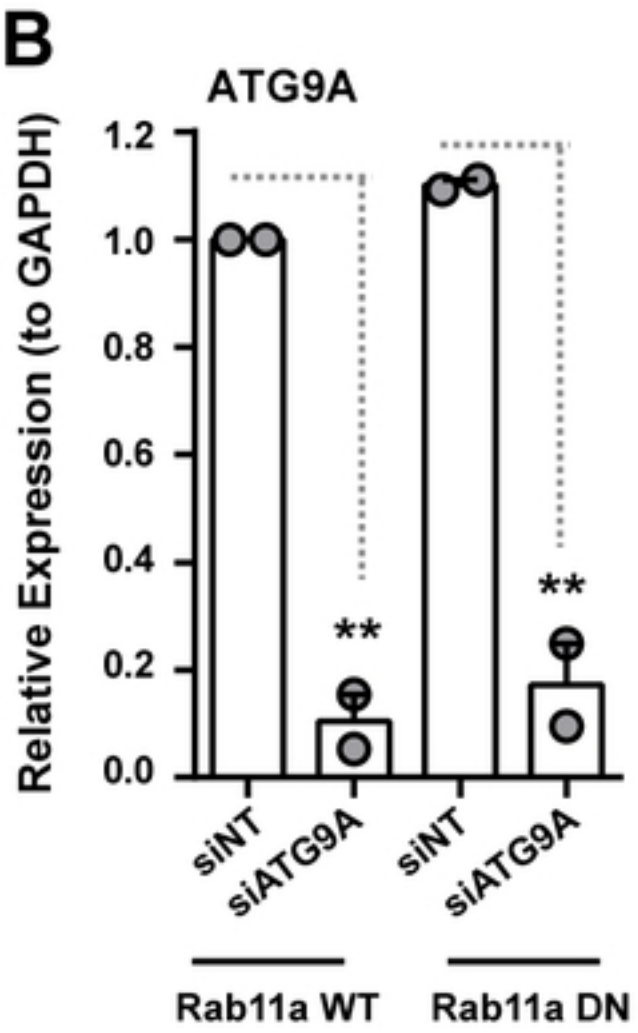

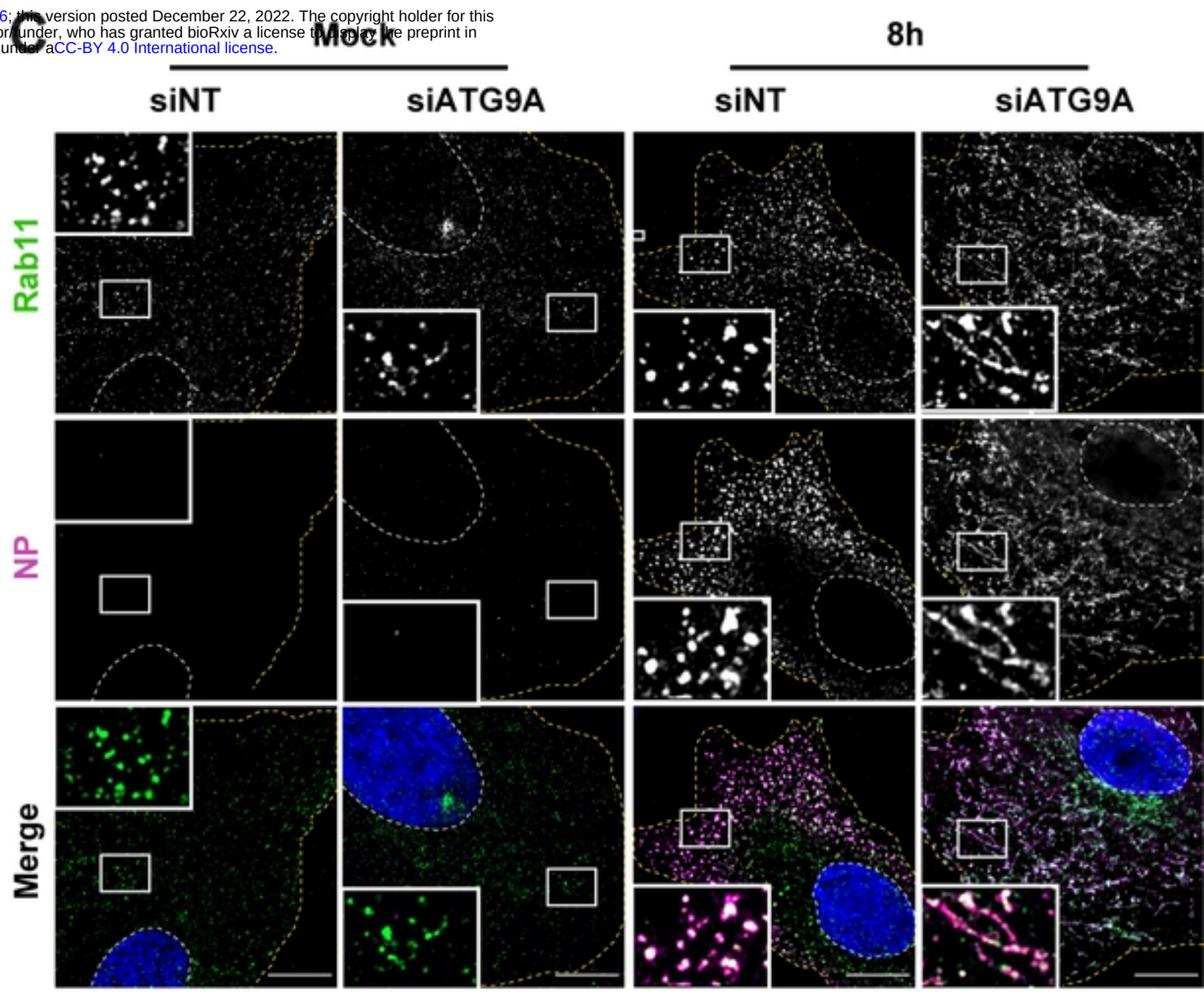

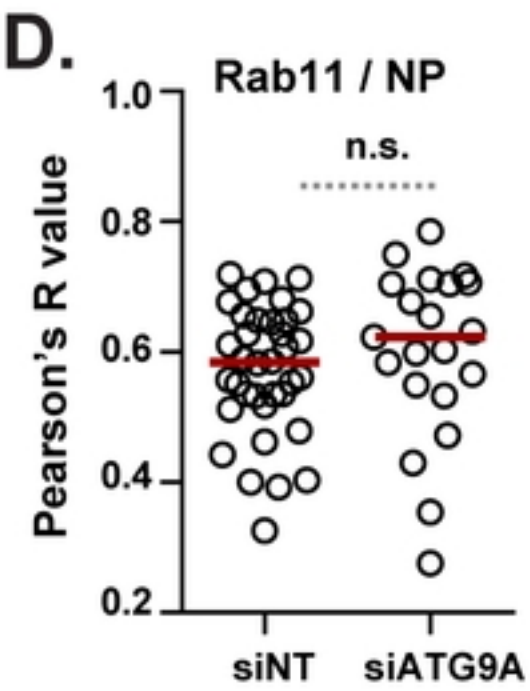

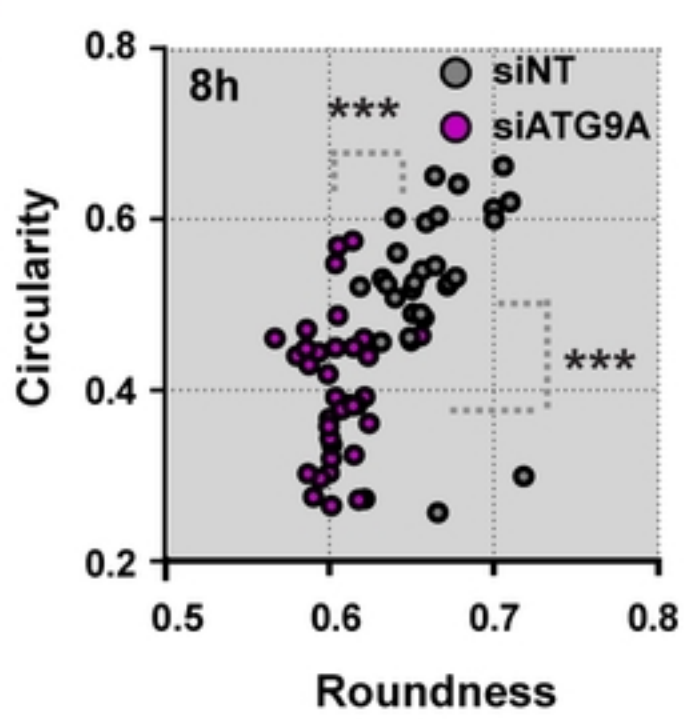

Figure 4

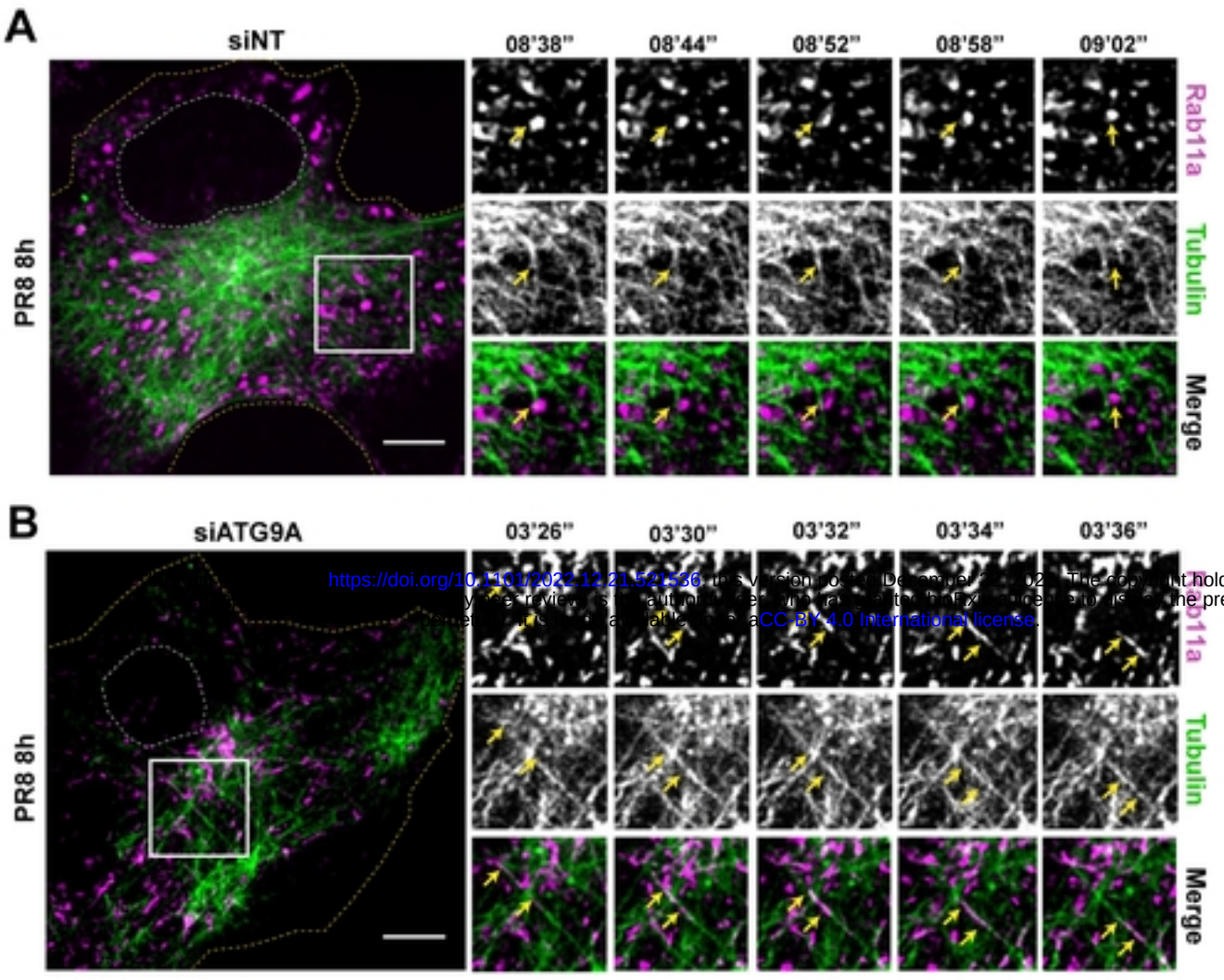

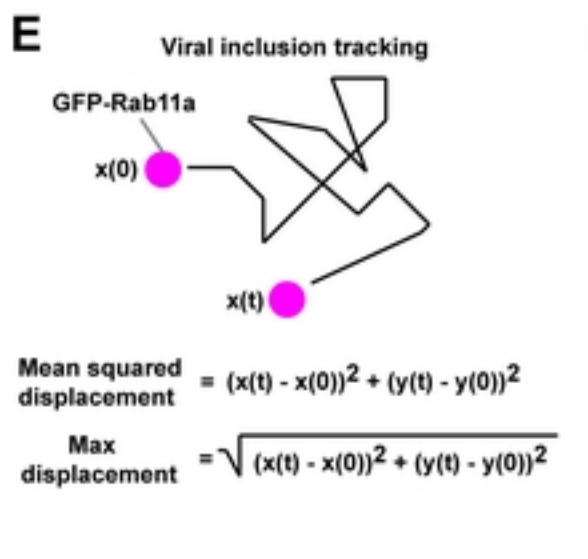

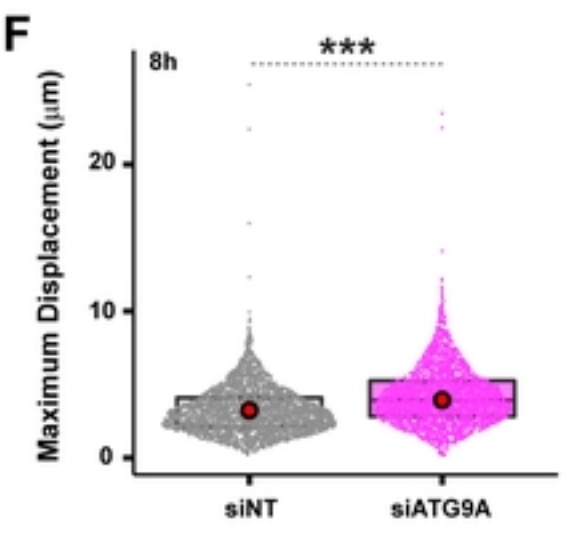

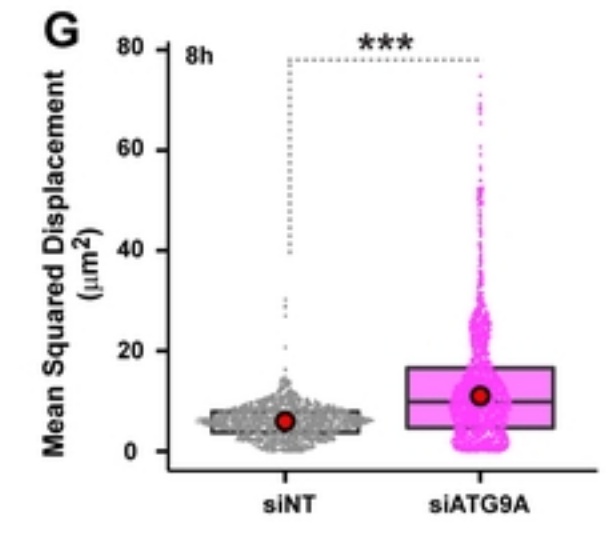

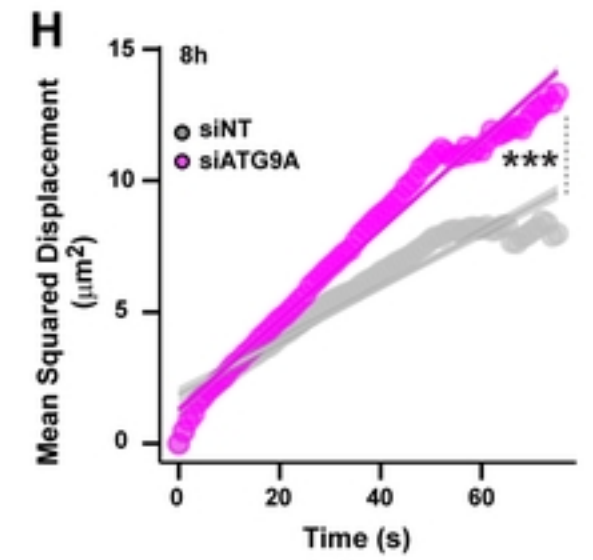

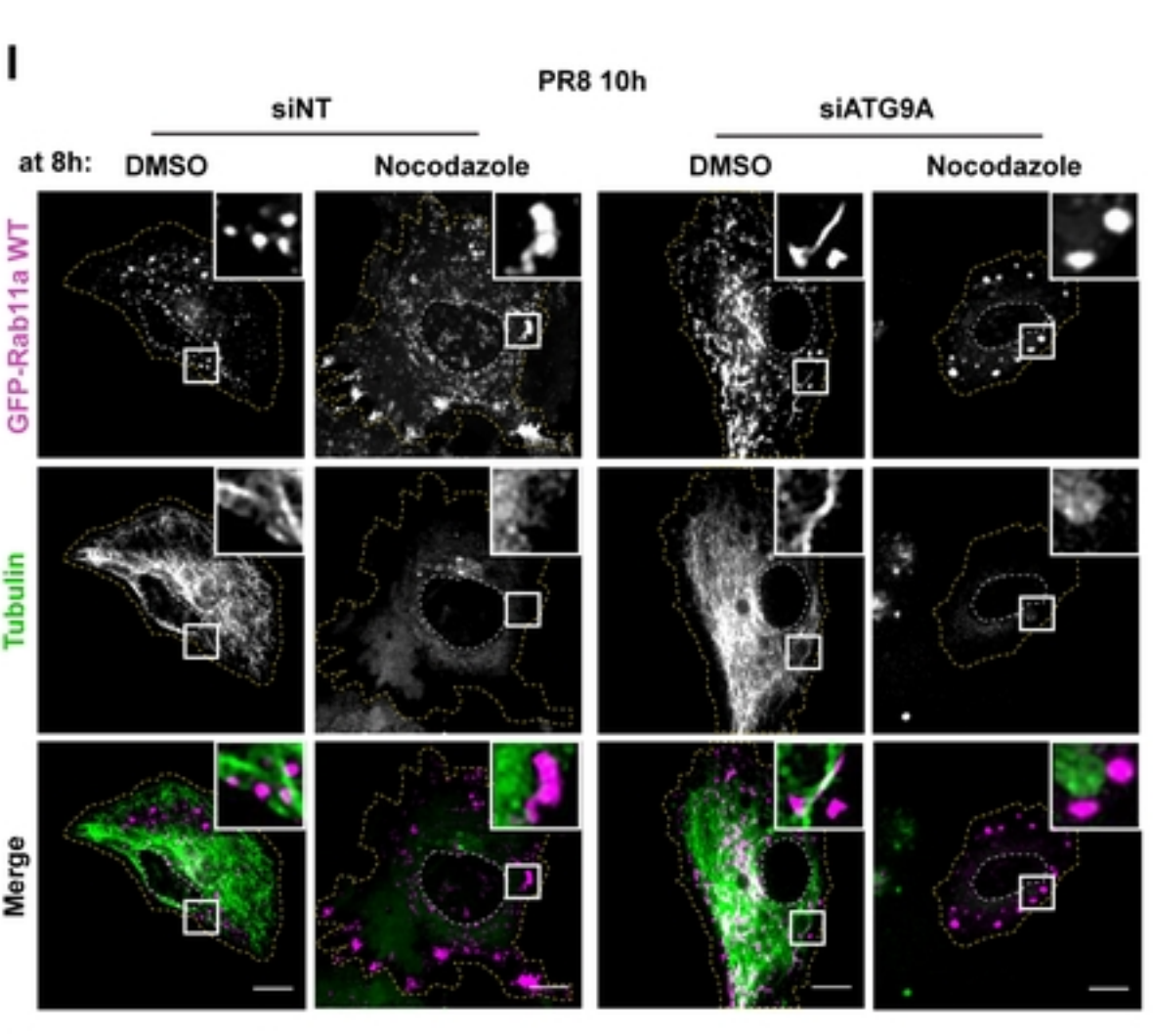

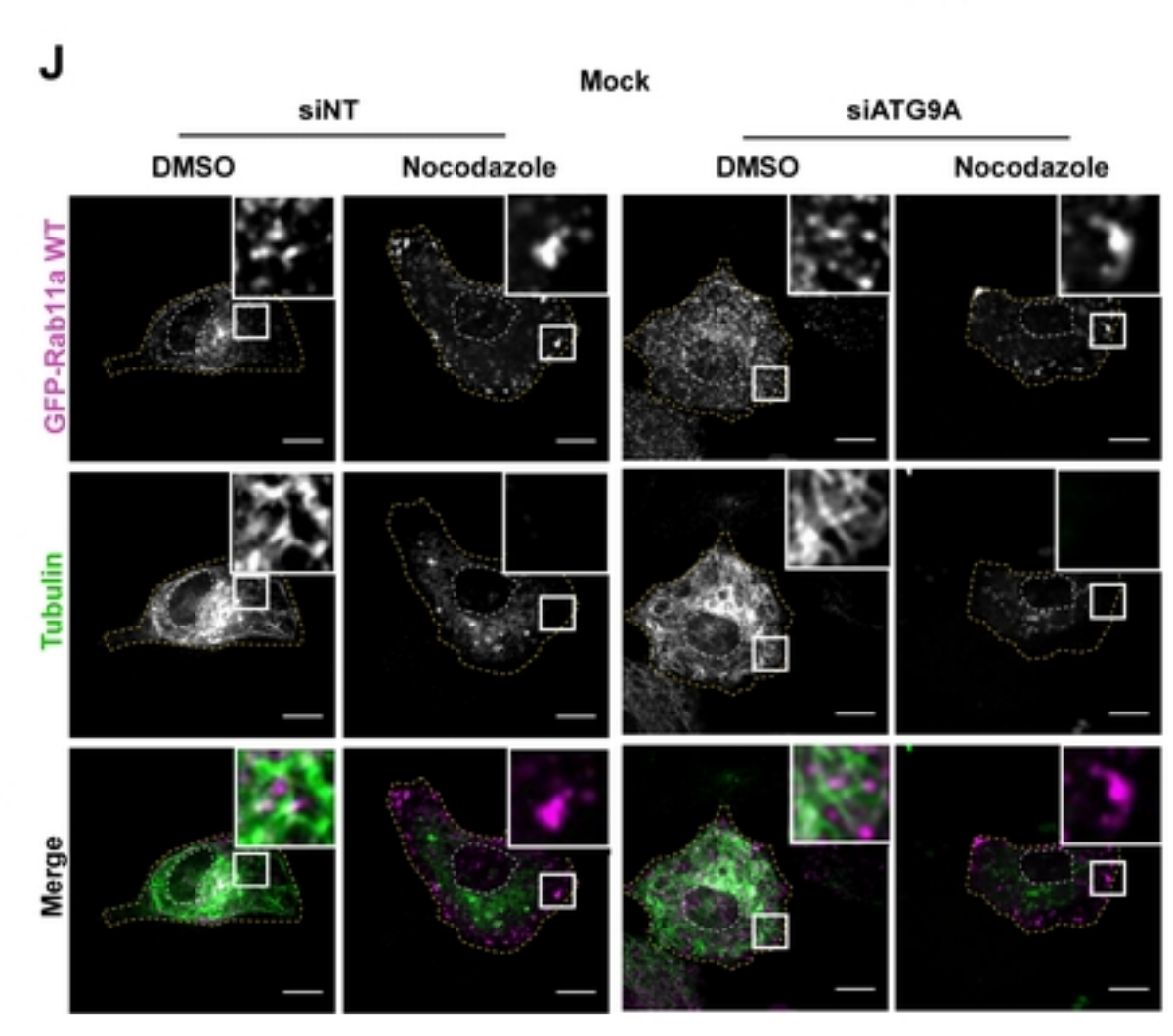

Figure 5

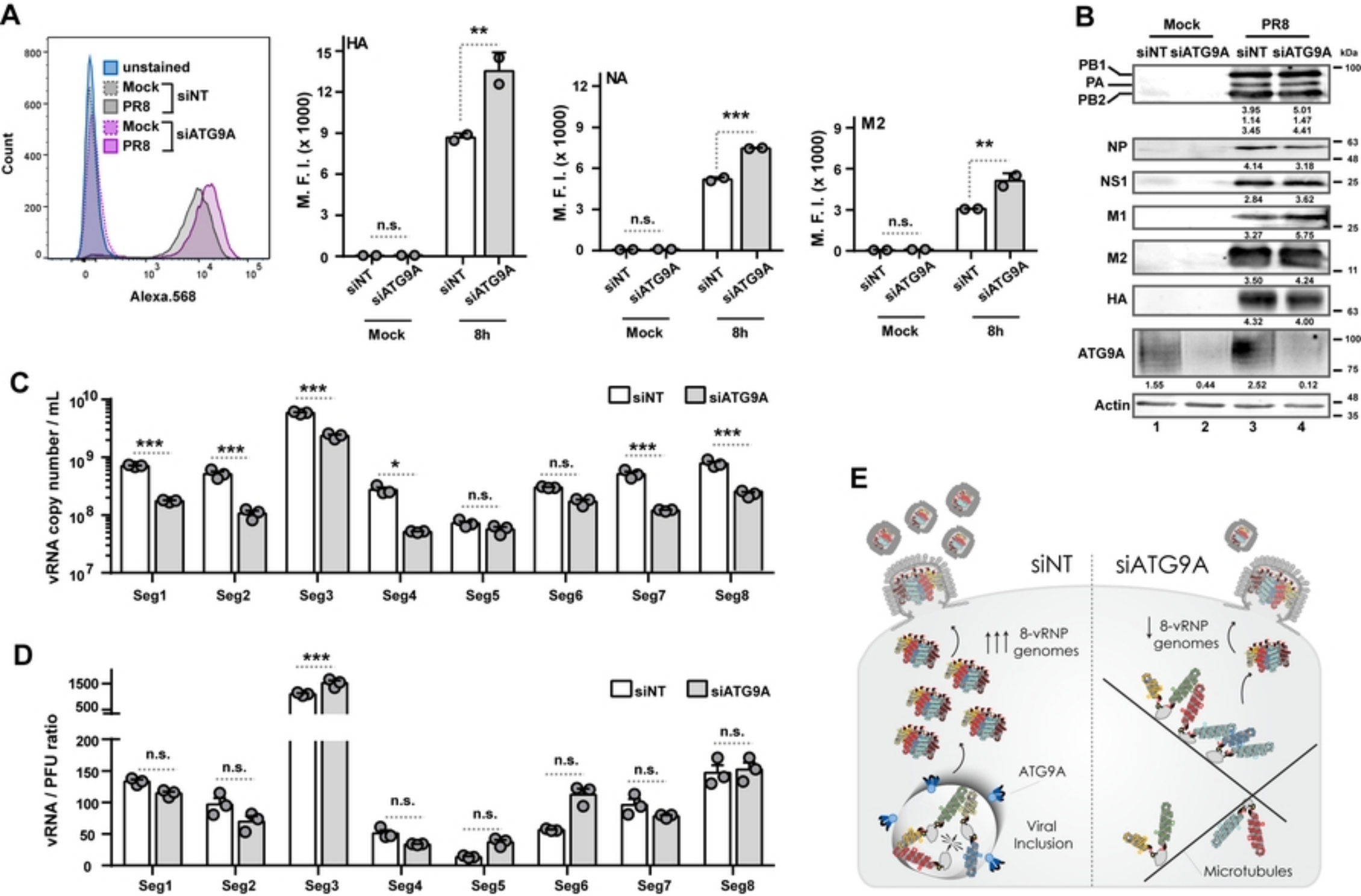
A
unstained
Mock
PR8
siNT
Mock
PR8
siATG9A
Count
Alexa.568
HA
NA
M2
M. F. I. (x 1000)
n.s.
**
***
siNT
siATG9A
Mock
8h
B
Mock
PR8
siNT siATG9A siNT siATG9A
kDa
PB1
PA
PB2
NP
NS1
M1
M2
HA
ATG9A
Actin
3.95 5.01
1.14 1.47
3.45 4.41
4.14 3.18
2.84 3.62
3.27 5.75
3.50 4.24
4.32 4.00
1.55 0.44 2.52 0.12
1 2 3 4
C
vRNA copy number / mL
siNT
siATG9A
Seg1
Seg2
Seg3
Seg4
Seg5
Seg6
Seg7
Seg8
D
vRNA / PFU ratio
E
siNT
siATG9A
8-vRNP genomes
ATG9A
Viral Inclusion
Microtubules

Figure 6

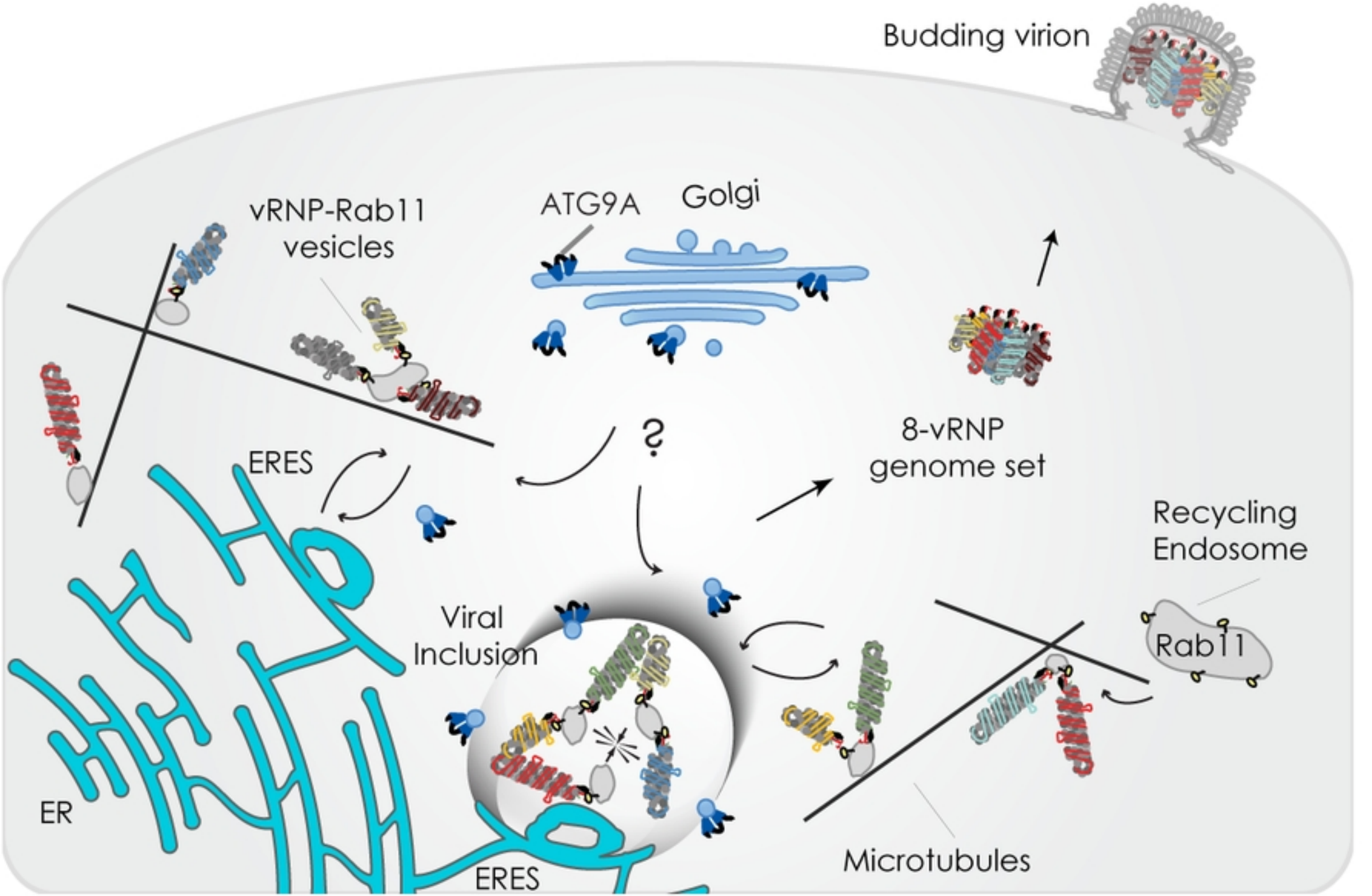
Budding virion
vRNP-Rab11
vesicles
ATG9A
Golgi
?
8-vRNP
genome set
ERES
Recycling
Endosome
Viral
Inclusion
Rab11
ER
ERES
Microtubules

Figure 7